JACS
JOURNAL OF THE AMERICAN CHEMICAL SOCIETY
pubs.acs.org/JACS
Article

Controlling Noncollinear Ferromagnetism in van der Waals Metal−Organic Magnets

Jem Pitcairn, Mario Antonio Ongkiko, Andrea Iliceto, Peter J. Speakman, Stuart Calder, Malcolm J. Cochran, Joseph A. M. Paddison, Cheng Liu, Stephen P. Argent, Andrew J. Morris, and Matthew J. Cliffe*

Cite This: https://doi.org/10.1021/jacs.4c04102

ABSTRACT: Van der Waals (vdW) magnets both allow exploration of fundamental 2D physics and offer a route toward exploiting magnetism in next generation information technology, but vdW magnets with complex, noncollinear spin textures are currently rare. We report here the syntheses, crystal structures, magnetic properties and magnetic ground states of four bulk vdW metal−organic magnets (MOMs): $FeCl_2$(pym), $FeCl_2$(btd), $NiCl_2$(pym), and $NiCl_2$(btd), pym = pyrimidine and btd = 2,1,3-benzothiadiazole. Using a combination of neutron diffraction and bulk magnetometry we show that these materials are noncollinear magnets. Although only $NiCl_2$(btd) has a ferromagnetic ground state, we demonstrate that low-field hysteretic metamagnetic transitions produce states with net magnetization in zero-field and high coercivities for $FeCl_2$(pym) and $NiCl_2$(pym). By combining our bulk magnetic data with diffuse scattering analysis and broken-symmetry density-functional calculations, we probe the magnetic superexchange interactions, which when combined with symmetry analysis allow us to suggest design principles for future noncollinear vdW MOMs. These materials, if delaminated, would prove an interesting new family of 2D magnets.

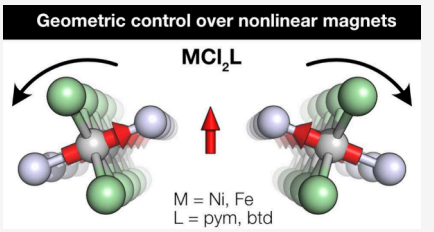

INTRODUCTION

The first reports of single layer ferromagnetism in the van der Waals (vdW) materials CrI_3[1] and $Cr_2Ge_2Te_6$[2] have sparked intensive efforts to realize the potential offered by two-dimensional magnetic materials for both the exploration of fundamental physics and the creation of new modalities for information technology.[3] The most widely studied families of vdW magnets are highly symmetric and as such typically possess collinear orderings.[1,4] The ability of more complex noncollinear magnetic order to generate new functional properties[5] is demonstrated by one of the few exceptions to this, NiI_2, for which there is evidence of spin-texture induced electrical polarization[6] and predictions of skyrmion phases.[7]

Rational design of these complex, noncollinear spin textures in vdW magnets remains an open challenge. Current strategies for inducing noncollinearity includes desymmetrization through Moiré twisting, e.g. noncollinear spin textures in four-layer CrI_3 stacks,[8] enhancing higher-order spin−orbit derived magnetic interactions,[9] and using lower-symmetry crystal structures. Extensive computational and theoretical searches for low-symmetry inorganic vdW materials have uncovered a handful of compounds which could host these states, such as the 1D type ordering in orthorhombic CrSBr[10,11] and noncollinear helical edge states in candidate Weyl semimetal WTe_2.[12−14]

Focusing solely on inorganic materials however overlooks one of the largest classes of known noncollinear magnets: coordination frameworks containing molecular ligands.[15] The use of molecular ligands typically lowers the structural symmetry, and hence permits the interactions required for noncollinearity, such as antisymmetric Dzyaloshinskii-Moriya interactions (DMI) or canting of the local single-ion anisotropy axes. There are now a number of vdW coordination frameworks with noncollinear magnetic structures;[16−20] however, their structural complexity also typically inhibits rational design or tuning of the magnetic interactions. Indeed, even in the highly tunable vdW metal imidazolates, MUV-1X(M) and MUV-8X(M), the deviations from collinearity cannot be readily controlled and are small.[21−23]

Metal dihalide N-heterocycles MX_2L are a modular family of materials, in which the organic ligand, L, and metal, M, can be varied while retaining the structural connectivity: metal halide chains connected by organic ligands into 2D rectangular layers (Figure 1a,b).[24−34] These materials are typically collinear antiferromagnets with the strongest superexchange interaction being along the MX_2 chain. The sign of the interaction depends most strongly on the metal: Ni, Co and Fe form ferromagnetic chains[28] and Cu and Cr form antiferromagnetic chains[26,30] The spatial relationship between MX_2 chains is

Received: March 23, 2024
Revised: June 17, 2024
Accepted: June 18, 2024

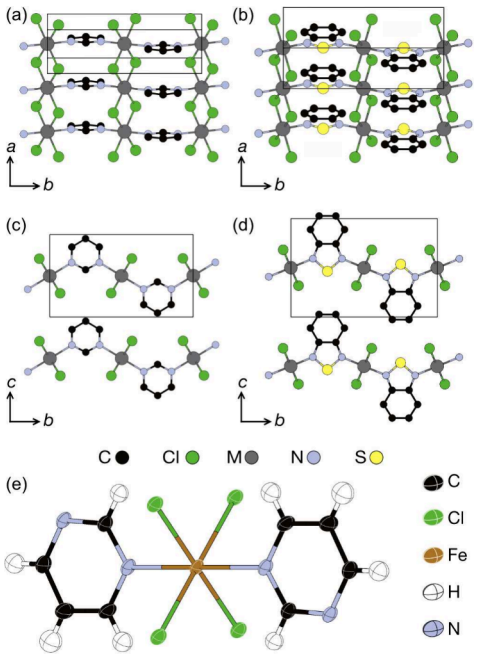

Figure 1. Crystal structure of $MCl_2(pym)$ viewed along the (a) *c*-axis and (c) a-axis and $MCl_2(btd)$ viewed along the (b) *c*-axis and (d) *a*-axis. The hydrogen atoms are omitted for clarity. (e) Oak Ridge Thermal Ellipsoid Plot (ORTEP) of $FeCl_2(pym)$ showing the coordination environment.

dictated by the organic ligand: the distance between chains is determined by ligand length[25] and the angle is controlled by the bonding geometry of the ligand (as in supramolecular cage chemistry).[31,35,36] The controllable nature of the structure means they are an ideal family to realize targetted magnetic phases: for example both $CuCl_2(btd)$ and $CrCl_2(pym)$ have proven ripe for investigations of 1D quantum magnetism.[26,31]

In this paper we report four noncollinear bulk van der Waals magnets, MCl_2L, where M = Ni and Fe, L = pyrimidine (pym) and 2,1,3-benzothiadiazole (btd). In each compound the noncollinearity leads to a net weak ferromagnetic moment within the layer with either a very large canting angle or large coercive field. We target these noncollinear states by connecting ferromagnetic MCl_2 chains with strong local anisotropy[28] using organic ligands with non 180° binding angles, thereby inducing interchain DMI interactions and ensuring the local single-ion anisotropy axes canted. We solve their structures using a combination of single-crystal X-ray diffraction (SCXRD), powder X-ray diffraction (PXRD) and powder neutron diffraction (PND), uncovering a low temperature structural phase transition in $FeCl_2(pym)$. Using bulk magnetic measurements and low temperature PND we determine their noncollinear magnetic ground states, showing that all four compounds possess weak ferromagnetic layers. These layers order antiferromagnetically in $FeCl_2(pym)$, $FeCl_2(btd)$ and $NiCl_2(pym)$, producing a fully compensated antiferromagnetic ground state, and order ferromagnetically in $NiCl_2(btd)$, producing a ferromagnetic ground state. Measurement of the magnetization as a function of field uncovers that all the antiferromagnetic compounds show low-field metamagnetic transitions, and both Ni compounds have very large hysteresis ($\mu_0 H_c$ > 1T, see Figure 4c,d, S13, S14) with $FeCl_2(pym)$ showing soft magnetic behavior, despite the antiferromagnetic ground state. Density-functional theory (DFT) calculations and diffuse scattering analysis allow us, together with symmetry arguments, to establish a hierarchy of interactions in these compounds thus rationalize their magnetic functions as arising from the competition between Heisenberg antiferromagnetic interchain exchange and spin−orbit coupling derived interactions. This allows us to suggest design rules for targetting noncollinear states in metal−organic layered magnets.

RESULTS

Synthesis. Phase pure microcrystalline bulk samples of $NiCl_2(btd)$ and $FeCl_2(btd)$ were synthesized by reacting $MCl_2{\cdot}nH_2O$ (n = 4 or 6 for M = Fe or Ni, respectively) and btd without solvent in a PTFE-lined autoclave at 200 °C for 72 h. Phase pure microcrystalline bulk samples of $NiCl_2(pym)$ and $FeCl_2(pym)$ were synthesized by mixing alcoholic solutions of $MCl_2{\cdot}nH_2O$ and pym. We found that less polar solvents favored the formation of the monopyrimidine $MCl_2(pym)$ phase over the bispyrimidine $MCl_2(pym)_2$[37,38] for both the Fe and Ni analogues. Aqueous synthesis produces the bispyrimidine phases,[37] whereas $FeCl_2(pym)$ can be readily synthesized in methanol and $NiCl_2(pym)$ in 2:1 ethanol-diethyl ether mixtures. Single crystals suitable for X-ray diffraction of $FeCl_2(pym)$ were grown by the slow diffusion of pym into a methanolic solution of $FeCl_2{\cdot}4H_2O$, but we were unable to grow single crystals of the other analogues.

Crystal Structures. Having grown diffraction-quality crystals of $FeCl_2(pym)$, we determined its high temperature orthorhombic structure by SCXRD at T = 120 K and the phase purity of the bulk microcrystalline sample was confirmed by PXRD at ambient temperature (Figure 1, S2, Table S2, S3). The low temperature monoclinic structure of $FeCl_2(pym)$ was determined by Rietveld refinement of PND data at T = 12.5K (Figure 2, Table S4). In the absence of crystals suitable for SCXRD measurements, the structure of $NiCl_2(pym)$ was determined by Rietveld refinement against PXRD data, using the structure of $FeCl_2(pym)$ as a starting model, as determined by SCXRD (Figure 1, S4). The monoclinic structures of $FeCl_2(btd)$ and $NiCl_2(btd)$ were determined by Rietveld refinement against PND data using DFT-optimized structures as a starting models (Figure 2, 1b and c). Simultaneous refinement of the nuclear and magnetic structure was undertaken for $FeCl_2(pym)$ and $FeCl_2(btd{-}d_4)$ against data collected at T = 2K. However, the same analysis was not performed for $NiCl_2(pym)$ and $NiCl_2(btd{-}d_4)$ as the signal-to-noise ratio of the magnetic Bragg peaks was not sufficient to constrain the model. We first describe the general features of the structures, before going on to describe the crystal structure and refinements in detail.

$FeCl_2(pym)$, $FeCl_2(btd)$, $NiCl_2(pym)$ and $NiCl_2(btd)$ all share a structural topology and have similar crystal structures. The M^{2+} (M = Fe, Ni) ions are coordinated by four Cl^- ligands and two N atoms from the pym and btd ligands, which form distorted MCl_4N_2 octahedra (Figure 1). The M octahedra edge-share through the Cl^- forming MCl_2 chains. At ambient temperature the asymmetric units of $FeCl_2(pym)$ and $NiCl_2(pym)$ contain only one Cl^-, so all four M− Cl bonds are equal in length, d_{Ni-Cl} = 2.458(2) Å and d_{Fe-Cl} = 2.492(5)Å (Table S2, S3). In the low temperature monoclinic phase of $FeCl_2(pym)$ the pyrimidine molecules are rotated about the *b*-direction, away from the *bc*-mirror plane, breaking the symmetry. This is accompanied by a small increase in the β-angle, 90° to 90.886(8)°, and a small rhombic distortion to

https://doi.org/10.1021/jacs.4c04102
J. Am. Chem. Soc. XXXX, XXX, XXX−XXX

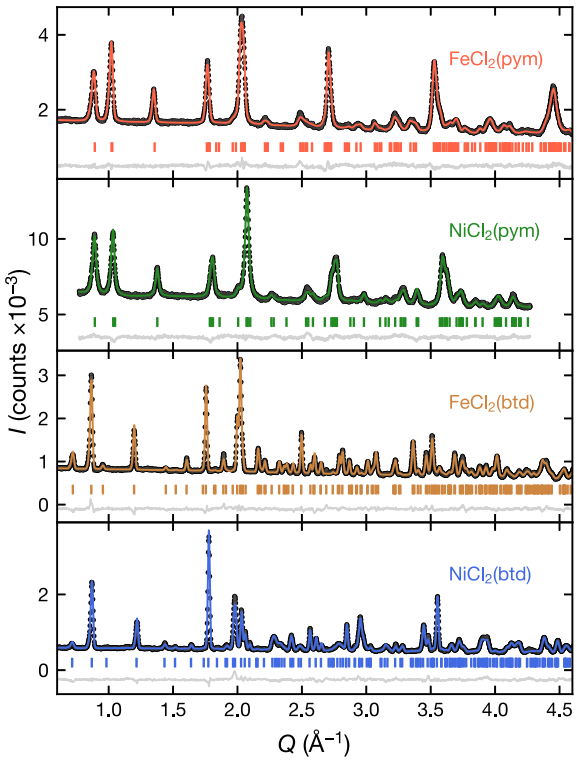

Figure 2. Rietveld refinement of the nuclear structures against powder neutron diffraction data. The measurement temperature for each data set is at $FeCl_2$(pym), T = 12.5 K; $FeCl_2$(btd), T = 5 K; $NiCl_2$(pym), T = 2 K and $NiCl_2$(btd) T = 2 K. For $NiCl_2$(pym) the first magnetic Bragg peak (Q = 0.70 Å^{-1}) was omitted and magnetic Bragg intensity at higher Q was negligible. For $NiCl_2$(btd) the magnetic Bragg intensity was fixed to values determined from magnetic Rietveld refinement (see Figure 6).

the coordination octahedra (Figure S6). Hence, the asymmetric unit of the low temperature $FeCl_2$(pym) phase contains two distinct Cl^-, so there are two M− Cl bonds with differing lengths, d_{Fe-Cl1} = 2.447(5)Å, d_{Fe-Cl2} = 2.450(5)Å. The asymmetric units of $FeCl_2$(btd) and $NiCl_2$(btd) also contain two distinct Cl^- and two M−Cl bonds with differing lengths, d_{Fe-Cl1} = 2.463(8)Å, d_{Fe-Cl2} = 2.554(8)Å, d_{Ni-Cl1} = 2.441(6)Å and d_{Ni-Cl2} = 2.528(6)Å (Table S3). Both of the Fe compounds show a larger distortion of the M− Cl bonds than their Ni analogues, suggesting that this distortion may be driven or enhanced by a weak Jahn−Teller distortion. The MCl_2 chains are connected into layers along the b-axis by μ-1,3-pym and μ-1,3-btd, but the bent ligands produce tilt angles between neighboring MCl_2 chains of 117(1)° through pym and 132(2)° through btd (Figure 1c and d). The orientations of the pym and btd alternate up-and-down along the b-axis (Figure 1c and d). The corrugated vdW layers stack on top of each other along c (Figure 1c and d). We have chosen the space group settings so that the a, b and c lattice parameters correspond to the equivalent chemical directions in these four new compounds and previously reported analogues:[26] the MCl_2 chains lying along the a, the btd or pym ligands along b and the vdW layers along c.

The structure of $FeCl_2$(pym) determined from SCXD data collected at T = 120 K and Rietveld refinement against PXRD data collected at ambient temperature shows it crystallizes in the orthorhombic space group $Pmmb$ (Table S2, Figure S2). However, refinement of the nuclear structure against PND data collected at T = 1.5, 12.5, and 25 K reveals that $FeCl_2$(pym) is in the monoclinic $P2_1/m$ space group at these temperatures (Figure 2, S2, Table S4). This structural phase transition can be seen in peak splitting of the peak at Q = 3.66 Å^{-1} and was confirmed by Rietveld refinement, where the monoclinic structure has a significantly improved fit and the cell angle refines away from 90°, β = 90.920(9)° (R_{wp} = 2.930, vs R_{wp} = 3.854 for β = 90°). We allowed the orientation of the pym to refine while keeping it as a rigid body. Our single crystal structure of $FeCl_2$(pym) was then used as a starting model for Rietveld refinement of the structure of $NiCl_2$(pym), initially against laboratory PXRD data (Figure S4), and then against PND data at T = 25 K. We found no evidence of a structural transition in $NiCl_2$(pym) down to 2 K.

The structures of $FeCl_2$(btd) and $NiCl_2$(btd) were determined by Rietveld refinement against PND data, using the DFT-optimized structures as a starting model (Figure S3 and S5). The DFT structures were produced by geometry-optimizing models derived from the previously reported structure of $CoCl_2$(btd).[32] In our refinements, in addition to the metal and halide, we were able to refine the position of the btd ligand as a rigid body, which rotates 2.9(1)° about the b-axis in $FeCl_2$(btd) and 1.3(1)° in $NiCl_2$(btd). The structure deviation from orthorhombic is much larger in these compounds than in low temperature $FeCl_2$(pym), with a markedly larger β angle, and the btd lies further from the bc-plane (Table S4, S5).

Magnetometry. Having synthesized bulk samples and determined the structure of these four vdW MOMs, we sought to understand their bulk magnetic properties. The variable-temperature susceptibility, $\chi(T)$, for each sample was measured under field cooled (FC) and zero-field cooled (ZFC) conditions in a 0.01 T dc field from 2 to 300 K, and the isothermal magnetization, $M(H)$, was measured at a range of temperatures between −5 T and 5 T for M = Fe and −14 T and 14 T for M = Ni.

Susceptibility. The $\chi(T)$ data for $FeCl_2$(pym), $FeCl_2$(btd) and $NiCl_2$(pym) show sharp cusps at 10.5(5) K, 3.8(2) K and 15.8(7) K respectively, which are characteristic of a transition to a long-range ordered antiferromagnetic state (Figure 3). In contrast, $NiCl_2$(btd) shows a bifurcation between the ZFC and FC $\chi(T)$ data at T = 17.5(5) K, indicative of ferromagnetic ordering (Figure 3d). The $\frac{d\chi}{dT}(T)$ data show discontinuities at these temperatures, providing further evidence of magnetic order (Figure S7d−S10d).

Fitting $\chi^{-1}(T)$ data of $FeCl_2$(pym) and $FeCl_2$(btd) each at T >100 K using the Curie−Weiss law gave effective moments of μ_{eff} = 5.9(2) μ_B for $FeCl_2$(pym) and μ_{eff} = 5.4(2) μ_B for $FeCl_2$(btd), consistent with high-spin S = 2 Fe^{2+} and unquenched orbital angular momentum (Table 1).[39−41] The Curie−Weiss temperatures were θ_{CW} = −2(1) K for $FeCl_2$(pym) and θ_{CW} = −1(3) K for $FeCl_2$(btd), indicating very small net antiferromagnetic interactions (Table 1, Figure S7c−S8c). $\chi^{-1}(T)$ was nonlinear for $FeCl_2$(btd) over the whole measured range and it was necessary to include an additional constant susceptibility term, χ_0 = 0.008(1) emu mol^{-1}, in the Curie−Weiss fit (Figure S8c).

Similarly, Curie−Weiss fitting to data measured above T >150 K gave an effective moment of μ_{eff} = 3.43(15) μ_B for $NiCl_2$(pym) and μ_{eff} = 3.32(16) μ_B for $NiCl_2$(btd) consistent with S = 1 Ni^{2+} (Table 1). Both Ni(II) materials had a positive Curie−Weiss temperatures indicative of net ferromagnetic

https://doi.org/10.1021/jacs.4c04102
J. Am. Chem. Soc. XXXX, XXX, XXX−XXX

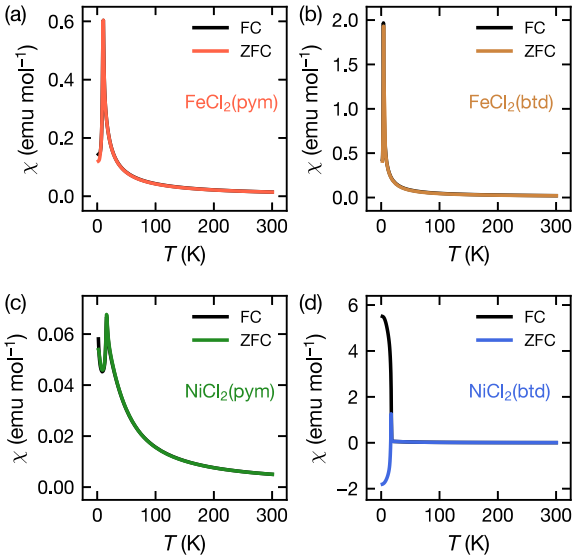

Figure 3. Magnetic susceptibility, $\chi(T)$, measurements in zero-field cooled (ZFC) and field cooled (FC) conditions from 2−300 K under a 0.01 T dc field for (a) $FeCl_2$(pym), (b) $FeCl_2$(btd), (c) $NiCl_2$(pym) and (d) $NiCl_2$(btd).

Table 1. Magnetic Property Parameters Determined from Magnetic Susceptibility Measurements[a]

	$FeCl_2$(pym)	$FeCl_2$(btd)	$NiCl_2$(pym)	$NiCl_2$(btd)
T_c (K)	10.5(5)	3.8(2)	15.8(7)	17.5(5)
C (emu K mol^{-1})	4.3(1)	3.6(2)	1.47(9)	1.39(2)
θ_{CW} (K)	−2(1)	−1(3)	9(4)	22(2)
μ_{eff} (μ_B)	5.9(2)	5.4(2)	3.43(15)	3.32(16)
g	2.40(8)	2.7(3)	2.42(5)	2.36(4)
M_r (μ_B)	0.28(1)*	–	0.127(5)†	0.088(2)†
H_C (T)	0.2(1)*	–	1.8(1)†	1.0(1)†
H_{c1} (T)	0.2(1)*	0.04(1)*	3.8(4)†	–
H_{c2} (T)	1.2(2)*	0.8(1)*	6.8(2)†	8.3(2)†
γ_{MH} (deg)	16.0(6)	–	9.1(4)	6.4(3)

[a] M_r and H_C were determined from data collected at (*) 2 K and (†) 1.8 K.

exchange, θ_{CW} = 9(4) K for $NiCl_2$(pym) and θ_{CW} = 22(2) K, for $NiCl_2$(btd), although $NiCl_2$(pym) is an antiferromagnet (Figure S9c, S10c). In all cases the presence of significant single-ion effects means that the Curie−Weiss temperature must be treated with caution.

Isothermal Magnetization. Our low temperature isothermal magnetization measurements in the ordered phases showed field-induced transitions in all samples and hysteresis in all but $FeCl_2$(btd) (Figure 4). In addition to a high field transition, an additional low field metamagnetic transition occurs in antiferromagnetic $FeCl_2$(pym), $FeCl_2$(btd) and $NiCl_2$(pym), but not in ferromagnetic $NiCl_2$(btd) (Table 1, Figure S13, S14).

The isothermal magnetization measurements of $NiCl_2$(pym) and $FeCl_2$(pym) have analogous shapes, though with features at very different fields. On the initial sweep from zero-field $M(H)$ increases linearly in the low field region with near constant susceptibility as expected for an antiferromagnet (Figure 4a and c). A sharp metamagnetic transition to a weak ferromagnetic state then occurs, H_{c1} = 0.2(1) T for $FeCl_2$(pym) and H_{c1} = 3.8(4) T for $NiCl_2$(pym). Finally a high field transition, likely to be a field polarized state, occurs

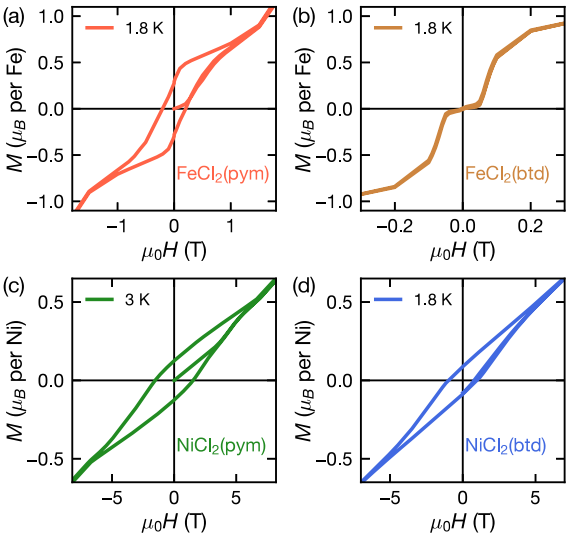

Figure 4. Isothermal magnetization measurements, $M(H)$, for (a) $FeCl_2$(pym) at 1.8 K between −2.6 T to 2.6 T, (b) $FeCl_2$(btd) at 1.8 K between −0.3 T to 0.3T, (c) $NiCl_2$(pym) at 3 K between −11 T to 11 T and (d) $NiCl_2$(btd) at 1.8 K between −7 T to 7 T.

at H_{c2} = 1.2(2) T for $FeCl_2$(pym) and H_{c2} = 6.8(2) T for $NiCl_2$(pym) (Figure S11c−e and S13c−e). There is considerable hysteresis in these transitions and the transition back to the antiferromagnetic state H_{c1} does not occur, leading to significant remnant magnetization: M_r = 0.28(1) μ_B for $FeCl_2$(pym) and M_r = 0.127(5) μ_B for $NiCl_2$(pym). This metamagnetic state has a considerable coercive field, H_C = 0.2(1) T for $FeCl_2$(pym) and H_C = 1.8(1) T for $NiCl_2$(pym) (Table 1, Figure 4a, S11a,b and S13a,b).

$FeCl_2$(btd) shares the initial metamagnetic transition H_{c1} = 0.04(1) T and high field transition H_{c2} = 0.8(1) T, which are accompanied by discontinuities in $\frac{dM}{dH}(H)$ (Figure S12c−e). However, we were not able to measure any hysteresis associated with either transition. As such, there is no remnant magnetization or coercive field, and the antiferromagnetic state can be easily reached by removing the applied field.

The ferromagnetic $NiCl_2$(btd) lacks the initial metamagnetic transition, but does show the high temperature field-polarized transition H_{c2} = 8 T (Figure S14c−e). It has a smaller hysteresis and remnant magnetization than the nominally antiferromagnetic $NiCl_2$(pym), M_r = 0.088(2) μ_B and H_C = 1.0(1) T at T = 1.8 K (Figure 4d, Figure S13, S14).

In no sample is saturation reached, strongly suggesting a noncollinear ground state. The angle between the spins and the averaged collinear axis is the canting angle, γ, which can be approximately determined from $M(H)$ data, γ_{MH} (Figure 5).

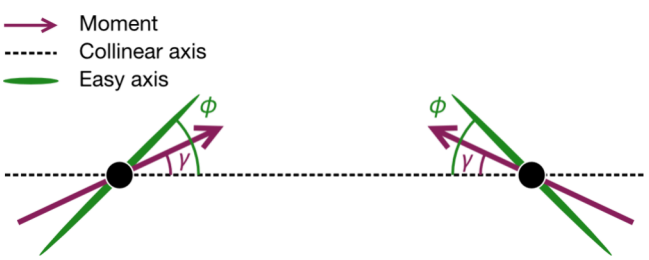

Figure 5. Definition of the canting angle γ and angle between the local easy-axes, ϕ and the collinear direction.

https://doi.org/10.1021/jacs.4c04102
J. Am. Chem. Soc. XXXX, XXX, XXX−XXX

Assuming a coplanar structure and a uniaxial ferromagnetic component, the measured powder-average of the remnant magnetization can be approximated by $M_r = \frac{1}{3}M_{\parallel} + \frac{2}{3}M_{\perp}$, where $M_{\perp} = 0$.[37,42] Hence, M_r can be multiplied by a factor of 3 to obtain the ferromagnetic moment along this axis, $M_{\parallel} = 3M_r$. Accordingly, the canting angle γ is

$$\sin \gamma_{\mathrm{MH}} = 3\frac{M_r}{M_s} \tag{1}$$

where M_s is the saturation magnetization (Figure 5). The saturation magnetization was determined using the g-factor from Curie–Weiss analysis $M_s = gS\mu_B$ (Table 1). Calculating the canting angle from the directly measured M_r gives γ_{MH} = 9.1(4)° for $NiCl_2$(pym) and 6.4(3)° for $NiCl_2$(btd). However, for $FeCl_2$(pym) the small coercive field means that nonlinear demagnetization, characteristic of domain structure, occurs rather than the linear dependence characteristic of continuous rotation of a canted spin. The directly measured value would therefore provide an underestimate of canting angle. To characterize just the intrinsic moment without contributions from domain structure, we determine a magnetization due to weak ferromagnetism by the extrapolation of the linear region of the hysteresis loop[43] from $M(\mu_0 H = 0.1)$ to zero field M_w = 0.44(1) μ_B, giving γ = 16.0(6)°. As there is no stable state for $FeCl_2$(btd) with a net moment, we are unable to carry out equivalent analysis.

Magnetic Diffraction. Our bulk magnetic measurements show strong evidence of long-range ordered magnetic ground states in all four compounds and so to determine the magnetic structure and correlations in their ground states, we carried out PND measurements using the HB-2A diffractometer at HFIR (ORNL). The magnetic structures were determined by refinement against data from which background and nuclear Bragg peaks were removed by subtraction of high temperature data in the paramagnetic regime. The magnetic Bragg peaks were indexed to determine the magnetic propagation vector and the possible irreducible representations (irreps) were determined using symmetry-mode analysis in the ISODISTORT software suite[44] which are denoted below in Miller and Love's notation.[45] Our Rietveld refinement of nuclear structures gave us the scale factor, which we then fixed for our Rietveld refinement of the magnetic structure using each irrep against the temperature subtracted data set. Having determined the magnetic structure using temperature-subtracted data, we were then able to carry out a joint magnetic and nuclear refinement for $FeCl_2$(pym) and $FeCl_2$(btd) (Table S5).

On cooling below T_C we find magnetic Bragg peaks for $FeCl_2$(pym) at T_N = 10.5(5) K, $FeCl_2$(btd) at T_N = 3.8(2) K, $NiCl_2$(pym) at T_N = 15.8(7) K and $NiCl_2$(btd) at T_C = 17.5(5) K (Figure S15). In the subtracted data sets we were able to isolate and index the magnetic Bragg peaks with propagation vectors, with the three antiferromagnets having a propagation vector $\mathbf{k} = 00\frac{1}{2}$ and the ferromagnetic $NiCl_2$(btd) having $\mathbf{k}$ = 000, confirming its ferromagnetic ground state (Figure 6, Table 2). We identified the possible irreps in each case and carried out Rietveld refinement of the magnetic structures using every irrep for each material. We found that only one irrep was consistent with the experimental data for each material: mB_1^+ for both $FeCl_2$(pym) and $FeCl_2$(btd); mZ_1^- for $NiCl_2$(pym); and $m\Gamma_2^+$ for $NiCl_2$(btd). We note that the observed magnetic structure for $FeCl_2$(pym) would require two different magnetic irreps were the high temperature orthorhombic phase used as the parent paramagnetic phase rather than the correct monoclinic phase (ESI Sec. S1.2).

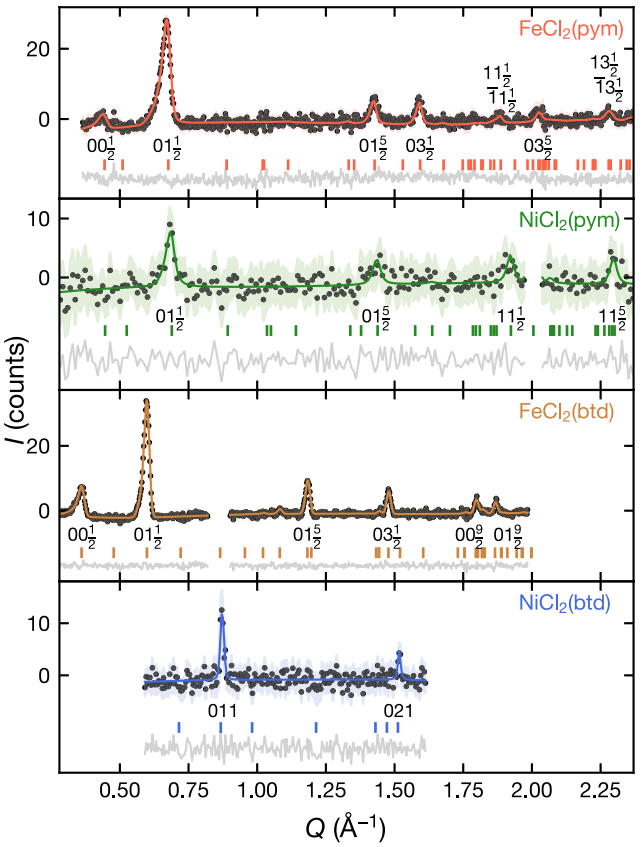

Figure 6. Rietveld refinement of the magnetic ground states against temperature subtracted neutron diffraction data. $FeCl_2$(pym): The model was refined against the $I_{1.5\ K} - I_{12.5\ K}$ data set over 0.36 < Q < 2.37 Å^{-1}. $FeCl_2$(btd): The model was refined against the $I_{1.5\ K} - I_{5\ K}$ data set over 0.26 < Q < 1.98 Å^{-1}. Data at 0.82 < Q < 0.09 Å^{-1} were omitted due to incomplete peak subtraction caused by thermal expansion. $NiCl_2$(pym): The model was refined against the $I_{2\ K} - I_{30\ K}$ data set over 0.29 < Q < 2.61 Å^{-1}. Data at 1.97 < Q < 2.04 Å^{-1} were omitted due to incomplete peak subtraction caused by thermal expansion. $NiCl_2$(btd): The model was refined against the $I_{1.5\ K} - I_{30\ K}$ data set over 0.59 < Q < 1.61 Å^{-1}. Data outside this range were omitted due to the absence of magnetic Bragg peaks and the presences of features arising from incomplete subtraction of structural Bragg peaks due to thermal expansion.

We were able to refine the moment directions and magnitudes freely for both iron compounds, but the lower signal-to-noise due to the smaller moment for nickel meant that we were only able to put an upper limit on the noncollinear component in the ordered moment for $NiCl_2$(pym) of $M \leq 1\ \mu_B$ and for $NiCl_2$(btd) of $M \leq 0.7\ \mu_B$. A canting angle of $\gamma \leq 30°$ for $NiCl_2$(pym) $\gamma \leq 23°$ for $NiCl_2$(btd) would be therefore challenging to detect in our neutron measurements. In particular, the additional peaks that would be a signature of this noncollinearity were too small to detect. For $NiCl_2$(pym) a noncollinear component along c is symmetry permitted and would produce Bragg intensity for $021_{\mathrm{mag.}}$. For $NiCl_2$(btd) a noncollinear component in the ac-plane is symmetry permitted and could produce Bragg intensity for the $001_{\mathrm{mag.}}$, $020_{\mathrm{mag.}}$ and $021_{\mathrm{mag.}}$ peak positions. We therefore constrained the moment to lie along the b-

https://doi.org/10.1021/jacs.4c04102
J. Am. Chem. Soc. XXXX, XXX, XXX−XXX

Table 2. Refined Magnetic Parameters from PND Analysis of the Magnetic Diffraction[a]

	$FeCl_2$(pym)	$FeCl_2$(btd)	$NiCl_2$(pym)	$NiCl_2$(btd)
Crystal system	Monoclinic	Monoclinic	Orthorhombic	Monoclinic
Magnetic space group (BNS)	P_a2_1/m	P_a2_1/m	P_ccca	$P2_1'/m'$
k-vector	$00\frac{1}{2}$	$00\frac{1}{2}$	$00\frac{1}{2}$	000
M_x (μ_B)	−3.096(65)	−3.434(30)	0*	0†
M_y (μ_B)	1.249(41)	1.643(22)	−2.012(70)	1.67(12)
M_z (μ_B)	1.653(19)	−1.103(19)	0†	0†
M_0 (μ_B)	3.726(99)	3.866(46)	2.012(70)	1.67(12)
γ_{ND} (deg)	19.6(5)	25.2(3)	≤30	≤23
C_{Cl}	FM	FM	FM	FM
$C_{pym/btd}$	ncAFM	ncAFM	(nc)AFM	(nc)AFM
C_{vdW}	AFM	AFM	AFM	AFM
T (K)	1.5	1.5	2	1.5
R_{wp}	29.303	14.320	65.703	63.114
GOF	0.905	0.806	0.473	5.892
λ (Å)	2.41	2.41	2.41	2.41

[a]The ordered moment is given in the Cartesian axes: $x = a_{nuc.}$, $y = b_{nuc.}$, $z = c_{nuc.} \times \sin\beta$. *Components prohibited by symmetry. †Components fixed to zero as no magnetic intensity detected in relevant reflections.

direction in $NiCl_2$(pym) and $NiCl_2$(btd). These refinements produced ordered moments in good agreement with those expected: M_0 = 3.726(99) μ_B for $FeCl_2$(pym), 3.866(46) μ_B for $FeCl_2$(btd), 2.012(70) μ_B for $NiCl_2$(pym) and 1.67(12) μ_B for $NiCl_2$(btd).

All four compounds have similar magnetic structures, with ferromagnetic correlations along the MCl_2 chains and primarily antiferromagnetic correlations along the *b*-direction. The interlayer correlations are antiferromagnetic, except for $NiCl_2$(btd). In the Ni compounds, the refined moments lie along the *b*-direction, though the canting is anticipated to occur along the *c* axis as this is allowed by symmetry. For $FeCl_2$(pym) and $FeCl_2$(btd) the moments primarily point along the *a* direction, but cant toward the *b* axis producing a net intralayer moment in this direction. This net moment is compensated for by the antiferromagnetic alignment with neighboring vdW layer (Figure 7a and b). A canting angle, γ_{ND} can be determined from the Rietveld refined structures:

$$\sin \gamma_{ND} = \frac{M_y}{M_0} \tag{2}$$

yielding γ_{ND} = 19.6(5)° for $FeCl_2$(pym) and 25.2(3)° for $FeCl_2$(btd).

We were also able to measure the paramagnetic diffuse scattering for $FeCl_2$(btd) at 5 and 10 K by subtracting data measured at 30 K (>6T_N) to account for structural scattering (Figure 8). By fitting this scattering using an effective-field model[46] we were able to extract superexchange interactions in the Heisenberg approximation, with the Hamiltonian

$$\mathcal{H} = -\frac{1}{2}\sum_{i,j} J_{ij}\mathbf{S}_i\cdot\mathbf{S}_j \tag{3}$$

where J_{ij} is isotropic superexchange for nearest neighbor, J_{Cl}, and next-nearest-neighbor, J_{btd} interactions, and $|S| = \sqrt{S(S+1)}$, and using a constant term to account for temperature dependent background scattering. The fit to these parameters show that J_{Cl} = 1.6(4) K is strongest and ferromagnetic, whereas the superexchange through the ligand, J_{btd} = −0.51(5) K is weaker and antiferromagnetic. Fitting with additional Heisenberg interaction terms, including J_{vdW}, J_{2Cl} (i.e., the next-nearest neighbor superexchange along the $FeCl_2$ chain), did not improve the quality of the fit and the refined values of these additional values were an order of magnitude smaller and zero within error. Refinement of a model with Ising spin degrees of freedom (moment directions fixed to those determined from refinement of the ground state) produced a less physical scale factor. The limited data quality means our measurements are only weakly sensitive to the single ion anisotropy and other spin−orbit derived interactions, and unfortunately prevented us from carrying out similar analysis for $FeCl_2$(pym) and the Ni(II) containing compounds.

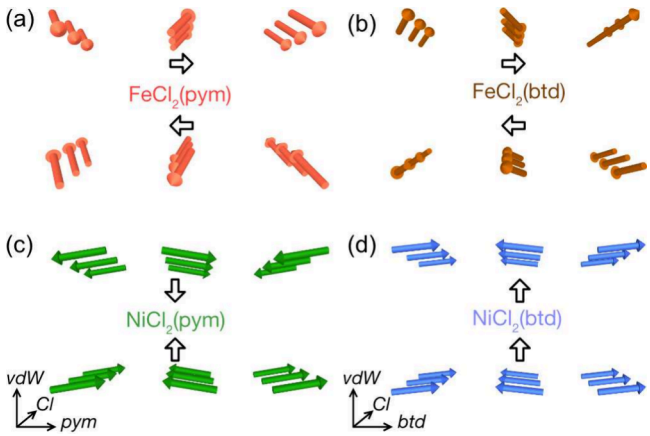

Figure 7. Schematic representation of the magnetic ground states of (a) $FeCl_2$(pym), (b) $FeCl_2$(btd), (c) $NiCl_2$(pym) and (d) $NiCl_2$(btd).

Density-Functional Theory. To get a deeper insight into the magnetic interactions in these materials we carried out first-principles DFT calculations. For each compound we relaxed the structure, using a primitive two atom cell, and calculated the exchange energies using the broken-symmetry approach.[47] The electronic structure and exchange energies were calculated using a collinear spin-polarized DFT Hamiltonian including a Hubbard *U* term using CASTEP,[48] including the MBD* dispersion correction.[49] We investigated using relativistic noncollinear DFT to prove the noncollinear

https://doi.org/10.1021/jacs.4c04102
J. Am. Chem. Soc. XXXX, XXX, XXX−XXX

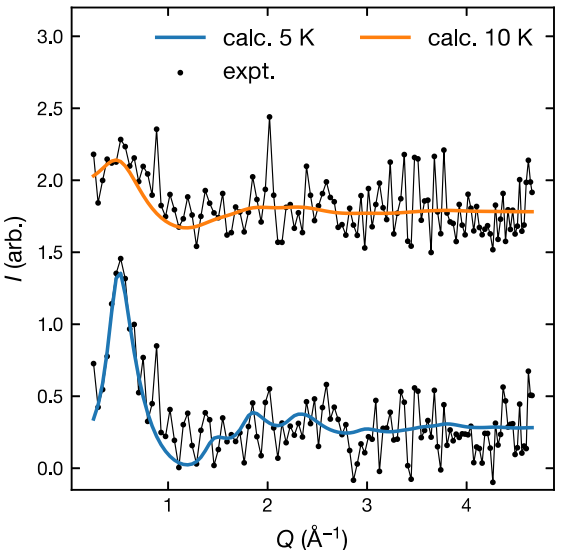

Figure 8. Magnetic diffuse scattering of $FeCl_2$(btd) fit using an effective field model.[46] Data obtained by temperature subtraction of data measured at 30 K.

magnetism found in these vdW MOMs (ESI Sec. S6.5), however these calculations were unable to provide any additional insight, due to the small energy-scales.

Geometry optimization of the primitive structures derived from single crystal X-ray diffraction data, $FeCl_2$(pym) and $CoCl_2$(btd)[32] with the transition metal substituted as appropriate, produced structures consistent with those obtained by Rietveld refinement: with typical mismatches of less than 1%, and the largest deviations of 3% found for $NiCl_2$(pym) (ESI Table S6). These calculations also found a small monoclinic distortion in $FeCl_2$(pym), as found in our low temperature Rietveld refinement of neutron diffraction data. Examination of the electronic structure, including density of states and band structure, revealed that the inclusion of a U parameter was essential to avoid unphysically delocalized states. We explored a range of U values from U = 0 to 10 eV for both systems,[50−52] determining that U = 2 eV for Fe and U = 6 eV for Ni were most appropriate. This correctly captured the experimentally observed insulating states for $FeCl_2$(pym) (E_g = 1.30 eV), $NiCl_2$(pym) (E_g = 2.48 eV) and $NiCl_2$(btd) (E_g = 1.52 eV), though we found that a metallic state results for $FeCl_2$(btd), likely due to strong electronic correlations on Fe(II). Our calculations for the Fe(II) compounds were very sensitive to U and did not reliably converge, particularly for $FeCl_2$(btd), and hence we have restricted our analysis of these calculations to structural features (additional calculations in ESI S6). We note that the chain like structure appears to afford significant delocalization along the a direction, particularly for btd containing compounds.

We created 2 × 1 × 2 supercells from the primitive cells to allow either configurations with either FM or AFM ordering along each of the three principal directions: M-Cl-M, M-organic-M, and M interlayer. We then calculated the energies of the eight possible magnetic configurations from these supercells and fitted their magnetic superexchange interactions to the magnetic Hamiltonian (eq 3, Table 3). We found that the superexchange was very sensitive to a U, with too small U producing unphysically large exchange.

We found that $NiCl_2$(pym) and $NiCl_2$(btd) both had ferromagnetic J_{Cl} and antiferromagnetic J_L consistent with our experimental ground states, bearing in mind the nonrelativistic nature of these calculations. Surprisingly, considering the experimental ground state, we found that $FeCl_2$(pym) consistently had antiferromagnetic exchange in both directions. This provides further evidence that the level of theory we are using to probe the electronic states of these Fe(II) compounds is not sufficient to accurately characterize the physics of these systems, perhaps due to the unquenched orbital moment in octahedral high spin Fe(II) and the relevance of both t_{2g} and e_g orbitals (which will have different localization but are treated with a single U in our calculations). Further details on our calculations on the iron compounds can be found in the ESI (Sec. S6). In all cases the interlayer interactions were zero within error. Focusing now on the Ni(II) compounds, we find that the interactions through pym are much more antiferromagnetic than through btd. This is consistent with the experimental Curie−Weiss temperatures, which are much less positive for $NiCl_2$(pym) (θ_{CW} = +9(4) K) than for $NiCl_2$(btd) (θ_{CW} = +22(2) K), though the presence of non-Heisenberg interactions prevents detailed quantitative comparison. Examination of the spin-density reveals that for both Ni(II) compounds e_g-type d-orbitals predominate, as predicted, and the ligand spin-density primarily lies within the σ-type orbitals, for Cl^-, pym and btd (Figure S25, S26).

Table 3. Calculated Magnetic Superexchange from Collinear PBE+MBD+U for $NiCl_2$(pym) and NiCl(btd) with U = 6 eV

	$NiCl_2$(pym)	$NiCl_2$(btd)
J_{Cl} (K)	29.5(4)	29.2(1)
J_L (K)	−29.0(4)	−9.7(1)
J_{vdW} (K)	−0.6(4)	0.0(1)

DISCUSSION

The lattice parameters and bond lengths in these compounds follow the expected trends. The a- and b-parameters are larger for the iron compounds than the nickel, in accordance with the ionic radii, and the a-parameter is also slightly larger for btd containing materials than the pym compounds due to a small induced distortion in the edge-sharing MCl_2 bridge. The b-parameter is significantly larger for the btd compounds than the pym compounds (≈7%) due to the μ-1,3-ligand being a five-membered ring in btd and a six-membered ring in pym. The c-parameter is significantly larger in the btd compounds than the pym, as the larger btd ligand separates the layers. The M− Cl− M bond angle is a key parameter in predicting J_{Cl},[53] and is approximately 94° in these compounds: 93.5° for $FeCl_2$(pym), 93.9° for $FeCl_2$(btd), 93.6° for $NiCl_2$(pym) and 94.9° for $NiCl_2$(btd). We see a decrease in the angle for $FeCl_2$(pym) in the high temperature phase to 91.6°, suggesting perhaps J_{Cl} also changes, though we find no evidence of this in our bulk magnetic data. These angles are broadly consistent with the binary halides $FeCl_2$ (92.2°[54]) and $NiCl_2$ (91.6°[55]), which also have nearest-neighbor ferromagnetic superexchange.[56,57]

Our neutron diffraction measurements, in combination with the bulk magnetometry, allow us to ascertain the magnetic ground state (Figure 7). We find that in all cases the moments are ferromagnetically correlated along the MCl_2 chains, which is consistent with the only magnetic structure of Ni(II) or Fe(II) MCl_2L analogues, $NiCl_2$(4,4′-bipyridine),[27] and as predicted by the Goodenough-Kamenari-Anderson rules.[58−60] Our PND measurements are sensitive to the canting angle γ,

https://doi.org/10.1021/jacs.4c04102
J. Am. Chem. Soc. XXXX, XXX, XXX−XXX

which are 19.6(5)° and 25.2(3)° for $FeCl_2$(pym) and $FeCl_2$(btd) (Table 2). For the Ni(II) compounds the small moment size means that we were only able to measure the most intense magnetic peaks, and so our neutron measurements instead put an effective ceiling on the canting angle. These values can be directly compared with those determined from the remnant magnetization, and are broadly consistent. The size of the canting angles for $FeCl_2$(pym) and $FeCl_2$(btd) is very large[15] and is comparable with some of the largest known canting angles.[37] This noncollinear magnetic order implies the presence of multiple competing interactions (as discussed below). The magnetic neutron diffraction also clearly establishes that although in all cases there is a (potential) net moment within the layers, only $NiCl_2$(btd) has ferromagnetic order, as the layers in $FeCl_2$(btd), $FeCl_2$(pym) and $NiCl_2$(pym) are antiferromagnetically coupled. $NiCl_2$(btd), $FeCl_2$(pym) and $NiCl_2$(pym) all show characteristics of ferromagnetism in applied field with significantly reduced M_s and M_r, which, together with magnetic ground state symmetries that permits noncollinearity, strongly suggests noncollinear ferromagnetism.

The compounds reported this manuscript are unusual vdW magnets as most are inorganic and collinear including ferromagnetic CrI_3,[1] $CrBr_3$,[61] $CrGeTe_3$,[2] and the antiferromagnetic $CrCl_3$,[62] MPS_3 (M = Mn, Fe, and Ni).[63−65] While inorganic ligands provide pathways for strong superexchange, their spherical symmetry also disfavors low symmetry structures that can produce noncollinear spin textures. The potential for low symmetry organic ligands to produce spin canting in vdW MOMs is clearly demonstrated by both these compounds and the MUV-1X(M) family of MOFs.[21−23] Many vdW magnets can be delaminated down to few layer form and this can lead to significant changes in their magnetic properties, including switching between ferro- and antiferromagnetic behavior.[1] If $MLCl_2$ can be delaminated into few- or monolayer form, we might anticipate similarities, as there appears to be a fine balance between interlayer ferromagnetism and antiferromagnetism.

$FeCl_2$(pym) and $NiCl_2$(pym) have the unusual combination of an antiferromagnetic ground state and magnetic hysteresis leading to remnant magnetism and a metastable zero-field ferromagnetic state. The presence of hysteresis is well-known around the metamagnetic transition, including even in canonical metamagnet $FeCl_2$[66] and in the related collinear $NiCl_2L$,[25] however the presence of metamagnetic hysteresis significant enough that the ferromagnetic state is stable without field is very rare, having been previously reported for two layered brucite cobalt hydroxides, $Co_2(OH)_3(NO_3)$ and $Co_4(OH)_2(O_2CC_6H_4CO_2)_3{\cdot}(NH_3)_{1.5}(H_2O)_{2.5}$.[67]

The coercive fields of $NiCl_2$(pym) (in its ferromagnetic phase) and $NiCl_2$(btd) are very large, both compared to other compounds and $FeCl_2$(pym). Indeed, H_C = 1.8 T at 2 K for $NiCl_2$(pym) is much larger than other vdW ferromagnets, even hard ferromagnets such as VI_3 (H_C = 0.9T).[68−70] The origin of this lies both with single-ion anisotropy and the magnetocrystalline anisotropy (MCA). As discussed below, Ni(II) is likely to have easy-axis, and Fe(II) easy-plane anisotropy, which suggests that the single-ion anisotropy contribution to coercivity will be larger for Ni(II). In addition, the net moment is out of plane for $NiCl_2$(pym) and $NiCl_2$(btd) and so will produce a larger MCA than the in plane net moment found for the Fe(II) compounds. This together likely explains the much larger coercive fields. It is notable that the related thiocyanate compound, $Ni(NCS)_2(pym)_2$ which has only M-pym-M connectivity, is also a weak ferromagnet with smaller, but still large H_C = 0.9T.[71,72] The direct analogues $Ni(NCS)_2$(pym) and $Fe(NCS)_2$(pym) are antiferromagnets, as the $M(NCS)_2$ chains are antiferromagnetic unlike the MCl_2 chains.[71,72]

The large canting found in $FeCl_2$(pym) parallels the compositionally similar (indeed, $FeCl_2$(pym) was found to be a common impurity) but structurally distinct $FeCl_2(pym)_2$, which has only Fe-pym-Fe connections and adopts a 3D diamondoid structure.[37] Despite the large differences in structure, these two compounds have similar magnetic properties, with M_r = 0.28(1)μ_B for $FeCl_2(pym)_2$ and M_r = 0.31(1)μ_B for $FeCl_2$(pym), suggesting that care is required in the analysis of magnetic susceptibility data to ensure purity. $FeCl_2$(pym) does however have an order of magnitude larger hysteresis, H_C = 0.2(1) T vs H_C = 0.015 T and a 2-fold larger magnetic ordering temperature, T_N = 10.5(5) K vs T_N = 6.5 K. The analogous diamondoid nickel compound $NiCl_2(pym)_2$ again has a slightly lower ordering temperature, T_N = 14.7(5) K, but is a collinear magnet with pseudo easy-axis anisotropy, as the easy-plane anisotropies of the NiN_4Cl_2 octahedra have a shared axis.[73]

The Curie−Weiss fitting and magnetic ordering temperature show interactions are stronger for $NiCl_2L$ than $FeCl_2L$. The limitations of powder susceptibility measurements mean that we are unable to disentangle robustly the three nearest neighbor Heisenberg interactions J_{Cl}, J_L and J_{vdW}) and spin−orbit derived terms (D, DMI interactions) through fitting of susceptibility data. For these layered materials, considering first Heisenberg superexchange only, T_c will depend most critically on the strongest two superexchange interactions ($\approx J_{Cl}+J_L$),[26] and the Curie−Weiss temperature on the mean interaction ($\approx J_{Cl}+J_L+J_{vdw}$), and so T_c and θ are expected to be similar. The single-ion anisotropy will have a complex effect, but typically leads to a reduction in θ and increase in T_c, explaining to some extent the observed discrepancies. Comparison with related compounds finds that both magnetic interactions tend to be stronger for Ni in both frameworks with only metal−ligand−metal connectivity[38] and frameworks with only metal-chloride-metal connectivity.[74,75]

The expected hierarchy of interactions predicts that superexchange through the MCl_2 chain is stronger than through the organic linker, which in turn is much stronger than between the layers, i.e., $J_{Cl} > J_{pym} \approx J_{btd} \gg J_{vdW}$. This ordering was observed in our previous quantitative inelastic neutron scattering investigations of the related $CrCl_2$(pym), where we found an order of magnitude separation between interactions.[26] Fitting of magnetic diffuse scattering does confirm this picture for $FeCl_2$(btd), with $J_{btd} \approx J_{Cl}/3$. Our DFT calculations suggest that the separation is less clear-cut for Ni(II) compounds, with $J_{pym} \approx J_{Cl}$ and $J_{btd} \approx J_{Cl}/2$.

Focusing on superexchange gives only a partial picture, as Heisenberg interactions alone will produce collinear order in a nonfrustrated magnet. Our preliminary DFT+U calculations including spin−orbit coupling were unable to shed significant extra light on the magnitude or directions of the key terms: however, we can produce simple guidelines from the model Hamiltonian, where we abstract away the strongest (Cl^-) and weakest interactions (vdW) to leave a 1D metal−ligand−metal chain. The two key interactions along this chain are the single ion anisotropy and the DMI, and this model has been studied extensively for single chain magnets.[76] In this case, as the true

https://doi.org/10.1021/jacs.4c04102
J. Am. Chem. Soc. XXXX, XXX, XXX−XXX

behavior is three-dimensional, we consider only the simplified static case. Both interactions, as they arise from spin−orbit coupling, are expected to be proportional to $\frac{g-2}{2}$. The observed structures require the competition between multiple different interactions, both Heisenberg and relatistivistic.

The DMI vector, **V**, which favors a pair of spins being perpendicular to both it and each other, for $NiCl_2$(pym) is normal to the pyrimidine ring by symmetry. This symmetry is broken in the monoclinic structures and instead is merely confined to the plane normal to the M−M vector. Nevertheless, as this symmetry breaking is not large, we can assume as a first approximation that the component of **V** within the ligand plane is small and that **V** lies along the plane normal. Within this approximation, the canting angle in the ordered ground state will be $\gamma = \frac{1}{2}\arctan(V/J_L)$. In this model, the DMI would be approximately 30% the size of superexchange for Ni and roughly equal to J in size for Fe if the canting is driven by DMI alone. These would be large values for the DMI interaction compared to other known compounds.[77]

Both Ni(II) and Fe(II) are expected to have significant single-ion anisotropy. In both cases the local ligand field environment can be thought of as "compressed" as the four weaker-field π-donor Cl^- ions lie in the equatorial plane, and the σ-donor N-heterocycles are axial. The use of the term compressed is by analogy with homoleptic complexes, where compression of two bonds relative to the others will cause a similar splitting of the d orbital levels, and does not imply anything about the relative bond lengths. For d^8 Ni(II) this leads to a strong easy-axis (Ising) type anisotropy,[42,78−81] and for d^6 Fe(II) this tends to produce an easy-plane (XY) type anisotropy.[78,82] As the true symmetry is below tetragonal, there will be additional small rhombic anisotropy, E, neglected in this approximate treatment. There are two key parameters: the angle between the easy-axis and the M−M vector, ϕ, and the strength of the single ion anisotropy D (Figure 5). ϕ = 0 and 90° corresponds to collinear anisotropy and hence will produce a collinear ground state, and ϕ = 45° favors a maximally canted state, which unusually has four degenerate ordered ground states.[83] For $NiCl_2$(btd), assuming the easy-axis is coincident with the N-M-N axis gives ϕ = 22.0(5)° and for $NiCl_2$(pym) this gives ϕ = 31.1(5)° due to the larger angle between the coordinating nitrogens in pym and btd. The derived canting angles are γ = 6.4(3)° for $NiCl_2$(btd) and γ = 9.1(3)° for $NiCl_2$(pym) (Table 1). These values rely on the validity of the assumptions made, and more accurate values could be obtained through single crystal magnetometry. Considering a Hamiltonian only containing single-ion anisotropy and Heisenberg AFM interactions for the Ni− L− Ni chain, analogous to that used in Pianet et al.,[83] gives $\frac{D}{J_L} = \frac{\sin(\gamma)}{\sin(\phi-\gamma)\cos(\phi-\gamma)}$. Using the experimental values this implies that D/J_L = 0.85(4) for $NiCl_2$(btd) and D/J_L = 0.90(3) for $NiCl_2$(pym), broadly consistent with D observed in similar materials.[79,80,84] The DMI and single-ion anisotropy terms will act cooperatively, and so the determined parameters thus correspond to estimates of the maxima rather than the central values. Our DFT calculations and Curie−Weiss analysis suggest that J_{pym} is significantly larger than J_{btd}, which would reduce the observed canting, suggesting that the noncollinear interactions (D and V) are in fact smaller for $NiCl_2$(btd).

The combination of easy-plane anisotropy and Heisenberg superexchange alone cannot produce spin canting in this model, and would instead select a unique spin direction: the intersection between the two staggered easy-planes. In these structures, the selected direction would correspond (assuming the easy-planes are oriented normal to the N-M-N axes) to spins oriented along the MCl_2 chain normal to the plane of the organic ligand. Indeed, the spins do largely lie on this direction for both $FeCl_2$(pym) and $FeCl_2$(btd). The deviation of the moment direction from this axis must arise from DMI interactions, rhombic anisotropy or higher order interactions neglected in this analysis.

Our estimates of the interactions creating the noncollinear spin structures only provide an initial understanding. Future measurements will give access to more precise quantification of the underlying origin of this phenomenon: allowing us to measure the relevant higher-order interactions directly. Inelastic neutron scattering measurements, whether on single crystals or powders, would provide precise measurements of the magnetic excitations and hence J_{Cl}, J_L, J_{vdW} and D, together with indications of deviations from these terms. High field EPR and single-crystal magnetometry measurements would accurately measure D and E. Calculations using dynamical mean-field theory (DMFT) and multiconfigurational methods (e.g., CASSCF) would allow for appropriate treatment of the electron correlation and spin−orbit contributions (respectively). Our model suggests that the noncollinearity in these materials can be enhanced through further desymmetrisation of the ligand field environment: replacing the N-heterocycle with a stronger field ligand or the bridging halide with a weaker field should increase the canting angle. Equally, the geometry of the organic ligand can be used to control the noncollinearity, and a ligand that tilts the metal halide chains more would produce a larger canting angle. In particular, we note that the tilt angle for pym is 32°: if this angle can be increased to ϕ = 45°, perhaps through using more bent ligands such as 3,6-diazacarbazole or 1-alkylpyrazolo[4,3-b]pyridine, a tetrastable state would be realizable.[83] This strategy for realizing noncollinear magnetism can be generalized to other metal−organic magnets where single ion anisotropy orientation can be anticipated.

CONCLUSION

We report here the syntheses, crystal structures, bulk magnetic properties and magnetic ground states of four vdW layered MOMs: $FeCl_2$(pym), $FeCl_2$(btd), $NiCl_2$(pym) and $NiCl_2$(btd). We show they all have noncollinear ground states with large canting and net magnetic moments within each layers, and that three of these materials have significant remnant magnetization. We use density-functional calculations together with consideration of model Hamiltonians to rationalize the magnetic properties of these materials, providing a framework for the design of new noncollinear vdW MOMs.

Although we show that the choice of transition metal is the key factor determining the magnetic character of these frameworks, we also demonstrate that the organic ligand has a key influence over the resulting properties. Substituting pym for btd changes the tilt-angle between MCl_2 chains, altering the tilt angles between chains and hence single-ion anisotropy axes, although the increased exchange in pym analogues partially counteracts this, the net result is an increased canting angle. The increased interlayer separation in btd analogues also reduces the transition magnetic fields. This suggests that the possibilities for chemical control available in MOMs will allow

https://doi.org/10.1021/jacs.4c04102
J. Am. Chem. Soc. XXXX, XXX, XXX−XXX

for tuning of spin texture, and hence potentially realizing functional properties such as magnetoelectricity[6] or skyrmion phases.[7]

This work suggests a few clear directions forward for these materials. Our results thus far, and their limitations, suggest that a deeper understanding of the spin−orbit derived interactions will be essential to further noncollinear vdW materials design. This spans both theory, including both higher level theoretical calculations (e.g., CASSCF or dynamical mean field theory) to understand in more detail the origin of the behavior, and experimental spectroscopic characterization of the behavior, including both inelastic neutron scattering and high field EPR investigations of the magnetic excitations. The promise of these materials in bulk crystalline form also prompts us to explore whether their properties can be maintained on few- or even monolayer scale and hence toward deeper integration of these materials into 2D devices.

EXPERIMENTAL SECTION

Synthesis. *$FeCl_2$(pym).* The reaction of $FeCl_2{\cdot}4H_2O$ (3.0 g, 15 mmol; Acros Organics, ≥99%) and pyrimidine (1.2 g, 15 mmol; Sigma-Aldrich, ≥98.0%) in 50 mL methanol (MeOH) rapidly precipitates an orange-brown microcrystalline powder. The $FeCl_2$(pym) product was then dried *in vacuo* giving a ca. 90% total yield. Crystals of sufficient size for X-ray diffraction studies (76 × 72 × 42 μm) were grown by vapor diffusion of pyrimidine (150 mg, 1.25 mmol; Sigma-Aldrich, ≥98.0%) into a concentrated solution of $FeCl_2$ in 1 mL MeOH (20 mg, 0.16 mmol; Acros Organics, 97%). The yield was 85%. The measured (calculated) elemental composition was C, 23.03% (23.2%); H, 1.98% (1.9%); and N, 13.01% (13.4%).

$FeCl_2$(btd). A PTFE-lined stainless-steel autoclave was charged with $FeCl_2{\cdot}4H_2O$ (795 mg, 4.00 mmol; Acros Organics, ≥99%) and 2,1,3-benzothiadiazole (579 mg, 4.25 mmol; Acros Organics, 98.0%) in the solid state. The autoclave was sealed and heated solvent-free in an oven at 200 °C for 72 h. Once heating was ceased, the reaction mixture was allowed to cool gradually to room temperature. This procedure, with 2,1,3-benzothiadiazole-d_4 (600 mg, 4.25 mmol; Sec.), was used to produce deuterated samples for neutron scattering studies. The yield was 93%. The measured (calculated) elemental composition was C, 25.20% (27.4%); H, 1.63% (1.5%); and N, 9.52% (10.6%).

$NiCl_2$(pym). The reaction of $NiCl_2{\cdot}6H_2O$ (173.2 mg, 0.729 mmol; Alfa Aesar, 98%) and pyrimidine (57.1 mg, 0.713 mmol; Sigma-Aldrich, ≥98.0%) in 30 mL ethanol (EtOH) rapidly precipitates a green microcrystalline powder. The $NiCl_2$(pym) product was washed in 3 × 20 mL EtOH and dried *in vacuo* giving a 91% total yield. The sample used for neutron-scattering measurements was synthesized by diffusion of pyrimidine (2.0 g, 25 mmol) into a solution of $NiCl_2{\cdot}6H_2O$ (5.9 g, 25 mmol) in 100 mL 2:1 EtOH-diethyl ether mix. The yield was 75%. The measured (calculated) elemental composition was C, 19.63% (22.9%); H, 2.00% (1.9%); and N, 11.11% (13.4%).

$NiCl_2$(btd). A PTFE-lined stainless-steel autoclave was charged with $NiCl_2{\cdot}6H_2O$ (951 mg, 4.00 mmol; Alfa Aesar, 98%) and 2,1,3-benzothiadiazole (579 mg, 4.25 mmol; Acros Organics, 98.0%) in the solid state. The autoclave was sealed and heated solvent-free in an oven at 200 °C for 72 h. Once heating was ceased, the reaction mixture was allowed to cool gradually to room temperature. This procedure, with 2,1,3-benzothiadiazole-d_4 (600 mg, 4.25 mmol; Sec.), was used to produce deuterated samples for neutron scattering studies. The yield was ca. 92%. The measured (calculated) elemental composition was C, 23.16% (27.1%); H, 3.60% (1.5%); and N, 9.22% (10.5%).

2,1,3-Benzothiadiazole-d_4. *o*-Phenylenediamine (2.0 g, 18.5 mmol; Sigma-Aldrich, >99%) and 20 wt % DCl/D_2O (0.40 g, Sigma-Aldrich, ≥99.5 atom % D) were refluxed in D_2O (50.0 g; Sigma-Aldrich, 99 atom % D) under N_2 atmosphere for 24 h. The reaction mixture was shielded from light while being heated. After cooling, the reaction mixture was extracted with dichloromethane (3 × 50 mL). The combined organic phases were dried over $MgSO_4$, filtered and concentrated *in vacuo*. The concentrated product, *o*-phenylenediamine-d_8 (1.70 g, 14.6 mmol) and triethylamine (6.36 g, 58.4 mmol) were stirred to dissolution in 50 mL dichloromethane. Thionyl chloride in dichloromethane (1 M concentration, 29.2 mL) was added dropwise to the solution at 0 °C under N_2 atmosphere in a foil wrapped flask. The solution was refluxed for 4 h under N_2 atmosphere and concentrated *in vacuo*. 2,1,3-benzothiadiazole-d_4 was purified by direct steam-distillation following addition of D_2O acidified to pH 1 with 20 wt % DCl/D_2O. The steam-distilled mixture was extracted with dichloromethane (3 × 50 mL) dried over $MgSO_4$ and filtered. Solvent was removed *in vacuo*, affording 2,1,3-benzothiadiazole-d_4 at 62% yield with 75% deuteration (1.27g, 9.05 mmol).

^{1}H NMR (400 MHz, $CDCl_3$, ppm, dioxane as an internal standard): δ_H 8.04−7.98 (m, 0.23H), 7.62−7.56 (m, 0.27H); ^{13}C NMR (101 MHz, $CDCl_3$, ppm): δ_C 154.78 (d, J = 5.5 Hz), 129.19 (dd, J = 12.5, 9.1 Hz), 121.50 (d, J = 11.2 Hz).

Powder X-ray Diffraction. PXRD data were collected using a PANalytical X'Pert Pro diffractometer equipped with monochromated Cu Kα_1 radiation (λ = 1.5406 Å). The tube voltage and current were 40 kV and 40 mA, respectively. Scans were performed from 2° to 80° on a zero background silicon crystal plate. Peak fitting, Pawley and Rietveld refinement were performed using Topas Academic v6.[85]

Single Crystal X-ray Diffraction. A diffraction-quality single crystal of $FeCl_2$(pym) was mounted on a polymer-tipped MiTeGen MicroMountTM using Fomblin (YR-1800 perfluoropolyether oil). The sample was cooled rapidly to 120 K in a stream of cold N_2 gas, using a Oxford Cryosystems open flow cryostat. Diffraction data were collected on an Oxford Diffraction GV1000 (TitanS2 CCD area detector, mirror-monochromated Cu−Kα radiation source; λ = 1.54184 Å, ω scans). Cell parameters were refined from the observed positions of all strong reflections and absorption corrections were applied using a Gaussian numerical method with beam profile correction (CrysAlisPro). The structure was solved and refined in Olex2[86] using SHELXT[87] and SHELXL,[88] respectively.

Magnetic Susceptibility. Magnetic property measurements were first carried out on a Quantum Design MPMS superconducting quantum interference device (SQUID; School of Chemistry, University of Nottingham, **a**). Additional isothermal magnetization measurements were carried out on a Quantum Design Dynacool Physical Property Measurement system (PPMS; Cavendish Lab, University of Cambridge, **b**). Data were corrected for the diamagnetism of the sample using Pascal's constants.[89]

$FeCl_2$(pym). **a**: A polycrystalline sample of $FeCl_2$(pym) (4.5 mg) was immobilized in eicosane (5.9 mg) and sealed in a gelatin capsule. Magnetic susceptibility measurements were performed under field cooled (FC) and zero-field cooled (ZFC) conditions in a 0.01 T *dc* field from 2 to 300 K. Isothermal magnetization measurements were performed at 2 K from 0 to 5 T to −5 to 5 T.

$FeCl_2$(btd-d_4). **a**: A polycrystalline sample of $FeCl_2$(btd) (18.82 mg) was immobilized in eicosane (14.73 mg) and sealed in a gelatin capsule. Magnetic susceptibility measurements were performed under field cooled (FC) and zero-field cooled (ZFC) conditions in a 0.01 and 2 T *dc* field from 2 to 300 K. Isothermal magnetization measurements were performed at 2 K from 0 to 5 T to −5 to 5 T.

$NiCl_2$(pym). **a**: A polycrystalline sample of $NiCl_2$(pym) (12.3 mg) was immobilized in eicosane (10.7 mg) and sealed in a gelatin capsule. Magnetic susceptibility measurements were performed under field cooled (FC) and zero-field cooled (ZFC) conditions in a 0.01 T *dc* field from 2 to 300 K.

b: A polycrystalline sample of $NiCl_2$(pym) (17.2 mg) was immobilized in cling film (7.3 mg). Isothermal magnetization measurements were performed at 1.8, 3, 4, and 8 K from 0 to 14 T to −14 to 14 T.

$NiCl_2$(btd-d_4). **a**: A polycrystalline sample of $NiCl_2$(btd) (8.63 mg) was immobilized in eicosane (9.22 mg) and sealed in a gelatin capsule. Magnetic susceptibility measurements were performed under field cooled (FC) and zero-field cooled (ZFC) conditions in a 0.01 T *dc* field from 2 to 300 K.

https://doi.org/10.1021/jacs.4c04102
J. Am. Chem. Soc. XXXX, XXX, XXX−XXX

b: A polycrystalline sample of $NiCl_2$(btd) (22.1 mg) was immobilized in cling film (4.8 mg). Isothermal magnetization measurements were performed at 1.8, 3, 4, 8, 16, and 32 K from 0 to 14 T to −14 to 14 T.

Powder Neutron Diffraction. Powder neutron diffraction measurements were carried out on the HB-2A neutron diffractometer at the High Flux Isotope Reactor (HFIR), Oak Ridge National Laboratory (ORNL).[90,91] A germanium monochromator was used to select λ = 2.41 Å from the Ge(113) reflection and λ = 1.54 Å from the Ge(115) reflection. The premono, presample, and predetector collimation was open-21'-12'. A pyrolytic graphite (PG) filter was placed before the sample to remove higher order reflections for λ = 2.41 Å. The samples were contained in a 6 mm diameter vanadium can and cooled in a liquid ^{4}He cryostat with an in situ 3-sample changer stick in the temperature range 1.5 to 300 K. The diffraction patterns were collected by scanning a 120° bank of 44 ^{3}He detectors in 0.05° steps to give 2θ coverage from 5° to 130°. The magnetic structures were determined by refinement against data from which background and nuclear Bragg peaks were removed by subtraction of data collected at $T > T_N$ from those collected at T = 1.5 or 2 K. The magnetic Bragg peaks were indexed to determine the magnetic propagation vector and then the allowed magnetic irreducible representations were determined using symmetry-mode analysis on the ISODISTORT software.[44] Using the scale factor determined from Rietveld refinement of the nuclear structure, and peak parameters determined from Pawley refinement of the nuclear structure, the direction and magnitude of the ordered moment for the subtracted data set were refined using TOPAS-ACADEMIC 6.0.[85]

$FeCl_2$(pym). Diffraction patterns were collected at T = 1.5, 12.5, and 25 K with λ = 2.41 Å for 4 h, 4h and 2h, respectively, and at T = 1.5 and 12.5 K with λ = 1.54 Å for 4 h each. Additional patterns were collected for 1 h at λ = 2.41 Å at intermediate temperature points T = 5, 6, 7, 8, 9, 9.5, 10, 10.5, 11, 12, 13, 14, and 15 K.

$FeCl_2$(btd-d_4). Diffraction patterns were collected at T = 1.5, 5, 10, and 30 K with λ = 2.41 Å for 3 h each. Additional data were collected with λ = 2.41 Å at Q = 0.60 Å^{-1} from T = 1.5 to 10 K in 0.5 K increments.

$NiCl_2$(pym). Diffraction patterns were collected at T = 2 and 30 K with λ = 2.41 Å for 3 h each. Additional data were collected with λ = 2.41 Å at Q = 0.68 Å^{-1} from T = 2 to 30 K in 3 K increments.

$NiCl_2$(btd-d_4). Diffraction patterns were collected at T = 1.5 and 30 K with λ = 2.41 Å for 3 h each. Additional data were collected with λ = 2.41 Å at Q = 0.87 Å^{-1} from T = 2 to 26 K in 1 K increments.

DFT Calculations. Calculations were carried out using the plane-wave density-functional theory code CASTEP version 23.1.[48] The PBE general gradient approximation exchange-correlation functional was used[92] with norm-conserving pseudopotentials from the built-in NCP19 library. Calculated exchange interactions were robust to changes in plane-wave cutoff energy for the basis set. van der Waals forces between each layer were described using the many-body semiemprical dispersion correction MBD*.[49] An effective on-site interaction parameter, $U_{eff} = U - J$, was necessary to impose a strong localization on the Fe and Ni d-states, where U is the on-site Coulomb term and J is the site exchange term. Ueff is applied as a correction to the total energy of the system,

$$\sum_I \left[\frac{U^I_{eff}}{2} \sum_{m,\sigma \neq m',\sigma'} n^{I\sigma}_m n^{I\sigma'}_{m'} - \frac{U^I_{eff}}{2} n^I (n^I - 1) \right] \quad (4)$$

where $n^{I\sigma}_m$ are localized orbital occupation numbers with atomic site index I, state index m, and spin σ.[93] $n^{I\sigma}_m$ is calculated as the projection of occupied Kohn−Sham DFT orbitals on a localized basis set. U_{eff} is set in CASTEP as a parameter that applies to all the orbitals within a given subshell (e.g., d-subshell).

A Monkhorst−Pack grid of k-points was used to integrate the Brillouin zone, with a k-point spacing finer than $2\pi \times 0.03$ Å^{-1} and with a plane-wave basis comprising plane-waves with energy up to 1500 eV. During the electronic minimization process a Gaussian smearing scheme was used with a smearing width of 0.2 eV. The geometry was optimized until forces were less than 0.05 eV/Å. The OptaDOS code in combination with the Matador high-throughput environment were used to generate the electronic band structures and density of states.[94−97] The C2X visualization tool was used to obtain the spin-density representations.[98]

■ ASSOCIATED CONTENT

Data Availability Statement

Additional research data for this article may be accessed at no charge and under CC-BY license at the University of Nottingham Research Data Management Repository (DOI: 10.17639/nott.7395).

Supporting Information

The Supporting Information is available free of charge at https://pubs.acs.org/doi/10.1021/jacs.4c04102.

Magnetic crystal structural information files (ZIP)

Discussion on the susceptibility of $FeCl_2$(btd) and magnetic symmetry analysis of $FeCl_2$(pym); additional powder X-ray and neutron diffraction data, refined lattice parameters, isothermal magnetization measurements, magnetic susceptibility analysis, refined magnetic ground states, UV−vis spectroscopy, additional details of DFT calculations (PDF)

Accession Codes

CCDC 2342368 contains the supplementary crystallographic data for this paper. These data can be obtained free of charge via www.ccdc.cam.ac.uk/data_request/cif, or by emailing data_request@ccdc.cam.ac.uk, or by contacting The Cambridge Crystallographic Data Centre, 12 Union Road, Cambridge CB2 1EZ, UK; fax: +44 1223 336033.

■ AUTHOR INFORMATION

Corresponding Author

Matthew J. Cliffe − *School of Chemistry, University Park, Nottingham NG7 2RD, United Kingdom;* orcid.org/0000-0002-0408-7647; Email: matthew.cliffe@nottingham.ac.uk

Authors

Jem Pitcairn − *School of Chemistry, University Park, Nottingham NG7 2RD, United Kingdom*

Mario Antonio Ongkiko − *School of Metallurgy and Materials, University of Birmingham, Birmingham B15 2TT, United Kingdom*

Andrea Iliceto − *School of Metallurgy and Materials, University of Birmingham, Birmingham B15 2TT, United Kingdom*

Peter J. Speakman − *School of Chemistry, University Park, Nottingham NG7 2RD, United Kingdom*

Stuart Calder − *Neutron Scattering Division, Oak Ridge National Laboratory, Oak Ridge, Tennessee 37831, United States*

Malcolm J. Cochran − *Neutron Scattering Division, Oak Ridge National Laboratory, Oak Ridge, Tennessee 37831, United States*

Joseph A. M. Paddison − *Neutron Scattering Division, Oak Ridge National Laboratory, Oak Ridge, Tennessee 37831, United States*

Cheng Liu − *Cavendish Laboratory, Department of Physics, University of Cambridge, Cambridge CB3 0HE, United Kingdom;* orcid.org/0000-0002-3509-951X

https://doi.org/10.1021/jacs.4c04102
J. Am. Chem. Soc. XXXX, XXX, XXX−XXX

Stephen P. Argent − *School of Chemistry, University Park, Nottingham NG7 2RD, United Kingdom;* orcid.org/0000-0002-3461-9675

Andrew J. Morris − *School of Metallurgy and Materials, University of Birmingham, Birmingham B15 2TT, United Kingdom;* orcid.org/0000-0001-7453-5698

Complete contact information is available at: https://pubs.acs.org/10.1021/jacs.4c04102

Notes

The authors declare no competing financial interest.

■ ACKNOWLEDGMENTS

M.J.C. and J.P. acknowledge funding from EPSRC Grant No. EP/X042782/1. High field magnetometry measurements were carried out using the Advanced Materials Characterisation Suite, funded by EPSRC Strategic Equipment Grant EP/M000524/1EPSRC. Computing resources were provided by the University of Birmingham's BlueBEAR HPC service and the Sulis Tier 2 HPC platform (EP/T022108/1), with networking support by CCP-NC (EP/T026642/1), CCP9 (EP/T026375/1), and UKCP (EP/X035891/1). A portion of this research used resources at the High Flux Isotope Reactor, a DOE Office of Science User Facility operated by the Oak Ridge National Laboratory. Andrew Jones is thanked for assistance with UV−visible spectroscopy measurements.

■ REFERENCES

(1) Huang, B.; Clark, G.; Navarro-Moratalla, E.; Klein, D. R.; Cheng, R.; Seyler, K. L.; Zhong, D.; Schmidgall, E.; McGuire, M. A.; Cobden, D. H.; Yao, W.; Xiao, D.; Jarillo-Herrero, P.; Xu, X. Layer-Dependent Ferromagnetism in a van Der Waals Crystal down to the Monolayer Limit. *Nature* **2017**, *546*, 270−273.

(2) Gong, C.; Li, L.; Li, Z.; Ji, H.; Stern, A.; Xia, Y.; Cao, T.; Bao, W.; Wang, C.; Wang, Y.; Qiu, Z. Q.; Cava, R. J.; Louie, S. G.; Xia, J.; Zhang, X. Discovery of Intrinsic Ferromagnetism in Two-Dimensional van Der Waals Crystals. *Nature* **2017**, *546*, 265−269.

(3) Wang, Q. H.; et al. The Magnetic Genome of Two-Dimensional van Der Waals Materials. *ACS Nano* **2022**, *16*, 6960−7079.

(4) McGuire, M. A. Crystal and Magnetic Structures in Layered, Transition Metal Dihalides and Trihalides. *Crystals* **2017**, *7*, 121.

(5) Kurebayashi, H.; Garcia, J. H.; Khan, S.; Sinova, J.; Roche, S. Magnetism, Symmetry and Spin Transport in van Der Waals Layered Systems. *Nat. Rev. Phys.* **2022**, *4*, 150−166.

(6) Song, Q.; Occhialini, C. A.; Ergeçen, E.; Ilyas, B.; Amoroso, D.; Barone, P.; Kapeghian, J.; Watanabe, K.; Taniguchi, T.; Botana, A. S.; Picozzi, S.; Gedik, N.; Comin, R. Evidence for a Single-Layer van Der Waals Multiferroic. *Nature* **2022**, *602*, 601−605.

(7) Amoroso, D.; Barone, P.; Picozzi, S. Spontaneous Skyrmionic Lattice from Anisotropic Symmetric Exchange in a Ni-halide Monolayer. *Nat. Commun.* **2020**, *11*, 5784.

(8) Xie, H.; Luo, X.; Ye, Z.; Sun, Z.; Ye, G.; Sung, S. H.; Ge, H.; Yan, S.; Fu, Y.; Tian, S.; Lei, H.; Sun, K.; Hovden, R.; He, R.; Zhao, L. Evidence of Non-Collinear Spin Texture in Magnetic Moiré Superlattices. *Nat. Phys.* **2023**, *19*, 1150−1155.

(9) Kim, C.; Kim, S.; Park, P.; Kim, T.; Jeong, J.; Ohira-Kawamura, S.; Murai, N.; Nakajima, K.; Chernyshev, A. L.; Mourigal, M.; Kim, S.-J.; Park, J.-G. Bond-Dependent Anisotropy and Magnon Decay in Cobalt-Based Kitaev Triangular Antiferromagnet. *Nat. Phys.* **2023**, *19*, 1624−1629.

(10) López-Paz, S. A.; Guguchia, Z.; Pomjakushin, V. Y.; Witteveen, C.; Cervellino, A.; Luetkens, H.; Casati, N.; Morpurgo, A. F.; von Rohr, F. O. Dynamic Magnetic Crossover at the Origin of the Hidden-Order in van Der Waals Antiferromagnet CrSBr. *Nat. Commun.* **2022**, *13*, 4745.

(11) Lee, K.; Dismukes, A. H.; Telford, E. J.; Wiscons, R. A.; Wang, J.; Xu, X.; Nuckolls, C.; Dean, C. R.; Roy, X.; Zhu, X. Magnetic Order and Symmetry in the 2D Semiconductor CrSBr. *Nano Lett.* **2021**, *21*, 3511−3517.

(12) Garcia, J. H.; Vila, M.; Hsu, C.-H.; Waintal, X.; Pereira, V. M.; Roche, S. Canted Persistent Spin Texture and Quantum Spin Hall Effect in WTe_2. *Phys. Rev. Lett.* **2020**, *125*, 256603.

(13) Tan, C.; Deng, M.-X.; Zheng, G.; Xiang, F.; Albarakati, S.; Algarni, M.; Farrar, L.; Alzahrani, S.; Partridge, J.; Yi, J. B.; Hamilton, A. R.; Wang, R.-Q.; Wang, L. Spin-Momentum Locking Induced Anisotropic Magnetoresistance in Monolayer WTe_2. *Nano Lett.* **2021**, *21*, 9005−9011.

(14) Zhao, W.; Runburg, E.; Fei, Z.; Mutch, J.; Malinowski, P.; Sun, B.; Huang, X.; Pesin, D.; Cui, Y.-T.; Xu, X.; Chu, J.-H.; Cobden, D. H. Determination of the Spin Axis in Quantum Spin Hall Insulator Candidate Monolayer WTe_2. *Phys. Rev. X* **2021**, *11*, 041034.

(15) Weng, D.-F.; Wang, Z.-M.; Gao, S. Framework-Structured Weak Ferromagnets. *Chem. Soc. Rev.* **2011**, *40*, 3157−3181.

(16) Rettig, S. J.; Thompson, R. C.; Trotter, J.; Xia, S. Crystal Structure and Magnetic Properties of Polybis(Formamide)Bis(μ-Formato)Cobalt(II): An Extended Two-Dimensional Square Lattice Material Which Exhibits Spontaneous Magnetization below 9 K. *Inorg. Chem.* **1999**, *38*, 1360−1363.

(17) Kawano, S.; Nakai, Y.; Matsugaki, N.; Achiwa, N.; Yamagata, K. Magnetic Structure of Monoclinic $Co(HCOO)_2 \cdot 2(NH_2)2CO$. *Physica B: Condensed Matter* **1995**, *213-214*, 265−267.

(18) Weng, Z.; Chen, Z.; Liang, F. Glycine-Templated Manganese Sulfate with New Topology and Canted Antiferromagnetism. *Inorg. Chem.* **2009**, *48*, 8703−8708.

(19) Wang, X.-Y.; Wang, L.; Wang, Z.-M.; Gao, S. Solvent-Tuned Azido-Bridged Co2+ Layers: Square, Honeycomb, and Kagomé. *J. Am. Chem. Soc.* **2006**, *128*, 674−675.

(20) Zheng, Y.-Z.; Xue, W.; Tong, M.-L.; Chen, X.-M.; Grandjean, F.; Long, G. J. A Two-Dimensional Iron(II) Carboxylate Linear Chain Polymer That Exhibits a Metamagnetic Spin-Canted Antiferromagnetic to Single-Chain Magnetic Transition. *Inorg. Chem.* **2008**, *47*, 4077−4087.

(21) López-Cabrelles, J.; Mañas-Valero, S.; Vitórica-Yrezábal, I. J.; Bereciartua, P. J.; Rodríguez-Velamazán, J. A.; Waerenborgh, J. C.; Vieira, B. J. C.; Davidovikj, D.; Steeneken, P. G.; van der Zant, H. S. J.; Mínguez Espallargas, G.; Coronado, E. Isoreticular Two-Dimensional Magnetic Coordination Polymers Prepared through Pre-Synthetic Ligand Functionalization. *Nat. Chem.* **2018**, *10*, 1001−1007.

(22) López-Cabrelles, J.; Mañas-Valero, S.; Vitórica-Yrezábal, I. J.; Šiškins, M.; Lee, M.; Steeneken, P. G.; van der Zant, H. S. J.; Mínguez Espallargas, G.; Coronado, E. Chemical Design and Magnetic Ordering in Thin Layers of 2D Metal-Organic Frameworks (MOFs). *J. Am. Chem. Soc.* **2021**, *143*, 18502−18510.

(23) López-Cabrelles, J.; Mañas-Valero, S.; Vitórica-Yrezábal, I. J.; Bereciartua, P. J.; Coronado, E.; Espallargas, G. M. A Fluorinated 2D Magnetic Coordination Polymer. *Dalton Trans.* **2022**, *51*, 1861−1865.

(24) Otieno, T.; Thompson, R. C. Antiferromagnetism and Metamagnetism in 1,4-Diazine and Pyridine Complexes of Nickel(II). *Can. J. Chem.* **1995**, *73*, 275−283.

(25) Cortijo, M.; Herrero, S.; Jiménez-Aparicio, R.; Matesanz, E. Modulation of the Magnetic Properties of Two-Dimensional Compounds $[NiX_2(N\text{-}N)]$ by Tailoring Their Crystal Structure. *Inorg. Chem.* **2013**, *52*, 7087−7093.

(26) Pitcairn, J.; Iliceto, A.; Cañadillas-Delgado, L.; Fabelo, O.; Liu, C.; Balz, C.; Weilhard, A.; Argent, S. P.; Morris, A. J.; Cliffe, M. J. Low-Dimensional Metal−Organic Magnets as a Route toward the S = 2 Haldane Phase. *J. Am. Chem. Soc.* **2023**, *145*, 1783−1792.

(27) Feyerherm, R.; Loose, A.; Lawandy, M.; Li, J. Crystal and Magnetic Structure of the Two-Dimensional Coordination Polymers $CoCl_2(bpy\text{-}d_8)$ and $NiCl_2(bpy\text{-}d_8)$. *Applied Physics A: Materials Science & Processing* **2002**, *74*, s778−s780.

(28) Lawandy, M. A.; Huang, X.; Wang, R.-J.; Li, J.; Lu, J. Y.; Yuen, T.; Lin, C. L. Two-Dimensional Coordination Polymers with One-Dimensional Magnetic Chains: Hydrothermal Synthesis, Crystal

Structure, and Magnetic and Thermal Properties of [MCl_2(4,4′-bipyridine)] (M = Fe, Co, Ni, Co/Ni). *Inorg. Chem.* **1999**, *38*, 5410−5414.
(29) de Campos, E. A.; Silva, N. J. O.; Shi, F.-N.; Rocha, J. Cobalt(II)-Pyrazine-Chloride Coordination Polymers: Synthesis, Reactivity and Magnetic Properties. *CrystEngComm* **2014**, *16*, 10439−10444.
(30) Butcher, R. T.; Landee, C. P.; Turnbull, M. M.; Xiao, F. Rectangular Two-Dimensional Antiferromagnetic Systems: Analysis of Copper(II) Pyrazine Dibromide and Dichloride. *Inorg. Chim. Acta* **2008**, *361*, 3654−3658.
(31) Papaefstathiou, G. S.; Tsohos, A.; Raptopoulou, C. P.; Terzis, A.; Psycharis, V.; Gatteschi, D.; Perlepes, S. P. Crystal Engineering: Stacking Interactions Control the Crystal Structures of Benzothiadiazole (btd) and its Complexes with Copper(II) and Copper(I) Chlorides. *Cryst. Grow. Des.* **2001**, *1*, 191−194.
(32) Papaefstathiou, G. S.; Perlepes, S. P.; Escuer, A.; Vicente, R.; Gantis, A.; Raptopoulou, C. P.; Tsohos, A.; Psycharis, V.; Terzis, A.; Bakalbassis, E. G. Topological Control in Two-Dimensional Cobalt-(II) Coordination Polymers by π-π Stacking Interactions: Synthesis, Spectroscopic Characterization, Crystal Structure, and Magnetic Properties. *J. Solid State Chem.* **2001**, *159*, 371−378.
(33) Haynes, J. S.; Sams, J. R.; Thompson, R. C. Magnetic and Spectroscopic Study of Pyrazine-Bridged Iron(II) Halide Complexes. *Inorg. Chem.* **1986**, *25*, 3740−3744.
(34) Ferraro, J. R.; Zipper, J.; Wozniak, W. Transition Metal(II) Complexes of the Azines. *Appl. Spectrosc.* **1969**, *23*, 160−164.
(35) Maurizot, V.; Yoshizawa, M.; Kawano, M.; Fujita, M. Control of Molecular Interactions by the Hollow of Coordination Cages. *Dalton Trans.* **2006**, *0*, 2750−2756.
(36) Zusai, K.; Kusaka, T.; Ishida, T.; Feyerherm, R.; Steiner, M.; Nogami, T. Magnetism of Pyrimidine-Bridged Metal(II) Halide Complexes. *Molecular Crystals and Liquid Crystals Science and Technology. Section A. Molecular Crystals and Liquid Crystals* **2000**, *343*, 127−132.
(37) Feyerherm, R.; Loose, A.; Ishida, T.; Nogami, T.; Kreitlow, J.; Baabe, D.; Litterst, F. J.; Süllow, S.; Klauss, H.-H.; Doll, K. Weak Ferromagnetism with Very Large Canting in a Chiral Lattice: Fe(Pyrimidine)$_2$Cl$_2$. *Phys. Rev. B* **2004**, *69*, 134427.
(38) Kreitlow, J.; Menzel, D.; Wolter, A. U. B.; Schoenes, J.; Süllow, S.; Feyerherm, R.; Doll, K. Pressure Dependence of $C_4N_2H_4$-Mediated Superexchange in $XCl_2(C_4N_2H_4)_2$ (X = Fe, Co, Ni). *Phys. Rev. B* **2005**, *72*, 134418.
(39) Kettle, S. F. A. *Physical Inorganic Chemistry: A Coordination Chemistry Approach*; WHFreeman: New York, 1996.
(40) Parks, G. A.; Akhtar, S. Magnetic Moment of Fe^{2+} in Paramagnetic Minerals. *Am. Mineral.* **1968**, *53*, 406−415.
(41) Figgis, B. N.; Lewis, J.; Mabbs, F. E.; Webb, G. A. The Magnetic Behaviour of Cubic Field $^5T_{2g}$ Terms in Lower Symmetry. *J. Chem. Soc. A* **1967**, 442−447.
(42) Blackmore, W. J. A.; et al. Determining the Anisotropy and Exchange Parameters of Polycrystalline Spin-1 Magnets. *New J. Phys.* **2019**, *21*, 093025.
(43) Gao, E.-Q.; Liu, P.-P.; Wang, Y.-Q.; Yue, Q.; Wang, Q.-L. Complex Long-Range Magnetic Ordering Behaviors in Anisotropic Cobalt(II)−Azide Multilayer Systems. *Chem. Eur. J.* **2009**, *15*, 1217−1226.
(44) Campbell, B. J.; Stokes, H. T.; Tanner, D. E.; Hatch, D. M. ISODISPLACE: A Web-Based Tool for Exploring Structural Distortions. *J. Appl. Crystallogr.* **2006**, *39*, 607−614.
(45) Cracknell, A. P.; Davies, B.; Miller, S. C.; Love, W. F. *Kronecker Product Tables*; IFI/Plenum: New York, 1979; Vol. *1*.
(46) Paddison, J. A. M. Spinteract: A Program to Refine Magnetic Interactions to Diffuse Scattering Data. *J. Phys.: Condens. Matter* **2023**, *35*, 495802.
(47) Ciofini, I.; Daul, C. A. DFT Calculations of Molecular Magnetic Properties of Coordination Compounds. *Coord. Chem. Rev.* **2003**, *238*−*239*, 187−209.
(48) Clark, S. J.; Segall, M. D.; Pickard, C. J.; Hasnip, P. J.; Probert, M. I. J.; Refson, K.; Payne, M. C. First Principles Methods Using CASTEP. *Z. Krist - Cryst. Mater.* **2005**, *220*, 567−570.
(49) Tkatchenko, A.; DiStasio, R. A.; Car, R.; Scheffler, M. Accurate and Efficient Method for Many-Body van Der Waals Interactions. *Phys. Rev. Lett.* **2012**, *108*, 236402.
(50) Mariano, L. A.; Vlaisavljevich, B.; Poloni, R. Biased Spin-State Energetics of Fe(II) Molecular Complexes within Density-Functional Theory and the Linear-Response Hubbard U Correction. *J. Chem. Theory Comput.* **2020**, *16*, 6755−6762.
(51) Lu, M.; Yao, Q.; Xiao, C.; Huang, C.; Kan, E. Mechanical, Electronic, and Magnetic Properties of NiX_2 (X = Cl, Br, I) Layers. *ACS Omega* **2019**, *4*, 5714−5721.
(52) Li, X.; Zhang, Z.; Zhang, H. High Throughput Study on Magnetic Ground States with Hubbard U Corrections in Transition Metal Dihalide Monolayers. *Nanoscale Adv.* **2020**, *2*, 495−501.
(53) Hatfield, W. E. Effect of Bridge Geometry on Exchange Coupling in Ligand-Bridged Copper(II) Dimers and Chains. *Comment. Inorg. Chem.* **1981**, *1*, 105−121.
(54) Vettier, C.; Yelon, W. B. The Structure of $FeCl_2$ at High Pressures. *J. Phys. Chem. Solids* **1975**, *36*, 401−405.
(55) Ferrari, A.; Braibanti, A.; Bigliardi, G. Refinement of the Crystal Structure of $NiCl_2$ and of Unit-Cell Parameters of Some Anhydrous Chlorides of Divalent Metals. *Acta Crystallogr.* **1963**, *16*, 846−847.
(56) Birgeneau, R. J.; Yelon, W. B.; Cohen, E.; Makovsky, J. Magnetic Properties of $FeCl_2$ in Zero Field. I. Excitations. *Phys. Rev. B* **1972**, *5*, 2607−2615.
(57) Lindgard, P. A.; Birgeneau, R. J.; Guggenheim, H. J.; Als-Nielsen, J. Spin-Wave Dispersion and Sublattice Magnetization in $NiCl_2$. *J. Phys. C: Solid State Phys.* **1975**, *8*, 1059.
(58) Goodenough, J. B. *Magnetism and the Chemical Bond*; Interscience Publishers John Wiley & Sons: New York, London, 1963.
(59) Kanamori, J. Superexchange Interaction and Symmetry Properties of Electron Orbitals. *J. Phys. Chem. Solids* **1959**, *10*, 87−98.
(60) Anderson, P. W. New Approach to the Theory of Superexchange Interactions. *Phys. Rev.* **1959**, *115*, 2−13.
(61) Tsubokawa, I. On the Magnetic Properties of a $CrBr_3$ Single Crystal. *J. Phys. Soc. Jpn.* **1960**, *15*, 1664−1668.
(62) McGuire, M. A.; Clark, G.; Kc, S.; Chance, W. M.; Jellison, G. E.; Cooper, V. R.; Xu, X.; Sales, B. C. Magnetic Behavior and Spin-Lattice Coupling in Cleavable van Der Waals Layered $CrCl_3$ Crystals. *Phys. Rev. Materials* **2017**, *1*, 014001.
(63) Long, G.; Henck, H.; Gibertini, M.; Dumcenco, D.; Wang, Z.; Taniguchi, T.; Watanabe, K.; Giannini, E.; Morpurgo, A. F. Persistence of Magnetism in Atomically Thin $MnPS_3$ Crystals. *Nano Lett.* **2020**, *20*, 2452−2459.
(64) Lançon, D.; Walker, H. C.; Ressouche, E.; Ouladdiaf, B.; Rule, K. C.; McIntyre, G. J.; Hicks, T. J.; Rønnow, H. M.; Wildes, A. R. Magnetic Structure and Magnon Dynamics of the Quasi-Two-Dimensional Antiferromagnet $FePS_3$. *Phys. Rev. B* **2016**, *94*, 214407.
(65) Wildes, A. R.; Stewart, J. R.; Le, M. D.; Ewings, R. A.; Rule, K. C.; Deng, G.; Anand, K. Magnetic Dynamics of $NiPS_3$. *Phys. Rev. B* **2022**, *106*, 174422.
(66) Chen, E. Y.; Dillon Jr, J. F.; Guggenheim, H. J. Magneto-Optical Studies of Metamagnetic Phase Transitions in $FeCl_2$. *AIP Conf. Proc.* **1974**, *18*, 329−333.
(67) Kurmoo, M. Ferrimagnetic and Metamagnetic Layered Cobalt (II)−Hydroxides: First Observation of a Coercive Field Greater than 5 T. *Philos. Trans. R. Soc. A* **1999**, *357*, 3041−3061.
(68) Tian, S.; Zhang, J.-F.; Li, C.; Ying, T.; Li, S.; Zhang, X.; Liu, K.; Lei, H. Ferromagnetic van Der Waals Crystal VI_3. *J. Am. Chem. Soc.* **2019**, *141*, 5326−5333.
(69) Kong, T.; Stolze, K.; Timmons, E. I.; Tao, J.; Ni, D.; Guo, S.; Yang, Z.; Prozorov, R.; Cava, R. J. VI_3—a New Layered Ferromagnetic Semiconductor. *Adv. Mater.* **2019**, *31*, 1808074.
(70) Son, S.; Coak, M. J.; Lee, N.; Kim, J.; Kim, T. Y.; Hamidov, H.; Cho, H.; Liu, C.; Jarvis, D. M.; Brown, P. A. C.; Kim, J. H.; Park, C.-H.; Khomskii, D. I.; Saxena, S. S.; Park, J.-G. Bulk Properties of the van Der Waals Hard Ferromagnet VI_3. *Phys. Rev. B* **2019**, *99*, 041402.

https://doi.org/10.1021/jacs.4c04102
J. Am. Chem. Soc. XXXX, XXX, XXX−XXX

(71) Wriedt, M.; Sellmer, S.; Näther, C. Thermal Decomposition Reactions as Tool for the Synthesis of New Metal Thiocyanate Diazine Coordination Polymers with Cooperative Magnetic Phenomena. *Inorg. Chem.* **2009**, *48*, 6896−6903.
(72) Wriedt, M.; Nather, C. Synthesis, Crystal Structure, and Thermal, Magnetic and Spectroscopic Properties of New Thiocyanato Transition Metal Coordination Polymers Based on Pyrimidine as Ligand. *Z. Anorg. Allg. Chem.* **2010**, *636*, 569−575.
(73) Vaidya, S.; Hernández-Melián, A.; Tidey, J. P.; Curley, S. P. M.; Sharma, S.; Manuel, P.; Wang, C.; Hannaford, G. L.; Blundell, S. J.; Manson, Z. E.; Manson, J. L.; Singleton, J.; Lancaster, T.; Johnson, R. D.; Goddard, P. A.Pseudo-easy-axis anisotropy in antiferromagnetic *S* = 1 diamond-lattice systems. *arXiv*, May 24, 2024. DOI: 10.48550/arXiv.2405.15623.
(74) Pokhodnya, K. I.; Bonner, M.; DiPasquale, A. G.; Rheingold, A. L.; Her, J.-H.; Stephens, P. W.; Park, J.-W.; Kennon, B. S.; Arif, A. M.; Miller, J. S. Structural and Magnetic Properties of MCl_2 (M = Fe, Mn, Co): Acetonitrile Solvates. *Inorg. Chem.* **2007**, *46*, 2471−2477.
(75) Witteveen, H. T.; Rutten, W. L. C.; Reedijk, J. Susceptibility Measurements on the Linear-Chain Compounds NiX_2L_2 with X = Cl, Br and L = Pyrazole, Pyridine. *J. Inorg. Nucl. Chem.* **1975**, *37*, 913−919.
(76) Pandit, R.; Tannous, C.; Krumhansl, J. A. Statistical Mechanics of a Classical One-Dimensional Canted Antiferromagnet. II. Solitons. *Phys. Rev. B* **1983**, *28*, 289−299.
(77) Huang, H.; Affleck, I. Susceptibility and Dzyaloshinskii-Moriya Interaction in the Haldane-gap Compound $Ni(C_2H_8N_2)_2NO_2(ClO_4)$. *Phys. Rev. B* **2004**, *69*, 184414.
(78) Oshio, H.; Nakano, M. High-Spin Molecules with Magnetic Anisotropy toward Single-Molecule Magnets. *Chemistry* **2005**, *11*, 5178−5185.
(79) Curley, S. P. M.; Scatena, R.; Williams, R. C.; Goddard, P. A.; Macchi, P.; Hicken, T. J.; Lancaster, T.; Xiao, F.; Blundell, S. J.; Zapf, V.; Eckert, J. C.; Krenkel, E. H.; Villa, J. A.; Rhodehouse, M. L.; Manson, J. L. Magnetic Ground State of the One-Dimensional Ferromagnetic Chain Compounds $M(NCS)_2(Thiourea)_2$ (M = Ni,Co). *Phys. Rev. Materials* **2021**, *5*, 034401.
(80) Manson, J. L.; et al. Spatially Anisotropic S = 1 Square-Lattice Antiferromagnet with Single-Ion Anisotropy Realized in a Ni(II) Pyrazine-N,N′-Dioxide Coordination Polymer. *Phys. Rev. B* **2023**, *108*, 094425.
(81) Wojnar, M. K.; Kundu, K.; Kairalapova, A.; Wang, X.; Ozarowski, A.; Berkelbach, T. C.; Hill, S.; Freedman, D. E. Field Design Enables Quantum Manipulation of Spins in Ni^{2+} Complexes. *Chem. Sci.* **2024**, *15*, 1374−1383.
(82) Rusbridge, E. K.; Peng, Y.; Powell, A. K.; Robinson, D.; Fitzpatrick, A. J. An Octahedral Tetrachlorido Fe(II) Complex with Aminopyrazinium Ligands from a Serendipitous Redox Synthesis Exhibiting Magnetic Exchange through Non-Covalent 3-D Architectures. *Dalton Trans.* **2018**, *47*, 7644−7648.
(83) Pianet, V.; Urdampilleta, M.; Colin, T.; Clérac, R.; Coulon, C. Magnetic Tetrastability in a Spin Chain. *Phys. Rev. B* **2016**, *94*, 054431.
(84) Blackmore, W. J. A.; et al. Magneto-Structural Correlations in Ni^{2+}−Halide···Halide−Ni^{2+} Chains. *Inorg. Chem.* **2022**, *61*, 141−153.
(85) Coelho, A. A. TOPAS and TOPAS-Academic: An Optimization Program Integrating Computer Algebra and Crystallographic Objects Written in C++. *J. Appl. Crystallogr.* **2018**, *51*, 210−218.
(86) Dolomanov, O. V.; Bourhis, L. J.; Gildea, R. J.; Howard, J. a. K.; Puschmann, H. OLEX2: A Complete Structure Solution, Refinement and Analysis Program. *J. Appl. Crystallogr.* **2009**, *42*, 339−341.
(87) Sheldrick, G. M. SHELXT − Integrated Space-Group and Crystal-Structure Determination. *Acta Cryst. A* **2015**, *71*, 3−8.
(88) Sheldrick, G. M. Crystal Structure Refinement with SHELXL. *Acta Crystallogr.* **2015**, *C71*, 3−8.
(89) Bain, G. A.; Berry, J. F. Diamagnetic Corrections and Pascal's Constants. *J. Chem. Educ.* **2008**, *85*, 532.
(90) Garlea, V. O.; Chakoumakos, B. C.; Moore, S. A.; Taylor, G. B.; Chae, T.; Maples, R. G.; Riedel, R. A.; Lynn, G. W.; Selby, D. L. The High-Resolution Powder Diffractometer at the High Flux Isotope Reactor. *Appl. Phys. A: Mater. Sci. Process.* **2010**, *99*, 531−535.
(91) Calder, S.; et al. A Suite-Level Review of the Neutron Powder Diffraction Instruments at Oak Ridge National Laboratory. *Rev. Sci. Instrum.* **2018**, *89*, 092701.
(92) Perdew, J. P.; Burke, K.; Ernzerhof, M. Generalized Gradient Approximation Made Simple. *Phys. Rev. Lett.* **1996**, *77*, 3865−3868.
(93) Tolba, S. A.; Gameel, K. M.; Ali, B. A.; A Almossalami, H.; Allam, N. K.; Tolba, S. A.; Gameel, K. M.; Ali, B. A.; A.Almossalami, H.; Allam, N. K. *Density Functional Calculations—Recent Progresses of Theory and Application*; IntechOpen, 2018.
(94) Morris, A. J.; Nicholls, R. J.; Pickard, C. J.; Yates, J. R. OptaDOS: A Tool for Obtaining Density of States, Core-Level and Optical Spectra from Electronic Structure Codes. *Comput. Phys. Commun.* **2014**, *185*, 1477−1485.
(95) Nicholls, R. J.; Morris, A. J.; Pickard, C. J.; Yates, J. R. OptaDOS - a New Tool for EELS Calculations. *J. Phys.: Conf. Ser.* **2012**, *371*, 012062.
(96) Yates, J. R.; Wang, X.; Vanderbilt, D.; Souza, I. Spectral and Fermi Surface Properties from Wannier Interpolation. *Phys. Rev. B* **2007**, *75*, 195121.
(97) Evans, M. L.; Morris, A. J. Matador: A Python Library for Analysing, Curating and Performing High-Throughput Density-Functional Theory Calculations. *J. Open Source Softw.* **2020**, *5*, 2563.
(98) Rutter, M. J. C2x: A Tool for Visualisation and Input Preparation for Castep and Other Electronic Structure Codes. *Comput. Phys. Commun.* **2018**, *225*, 174−179.

https://doi.org/10.1021/jacs.4c04102
J. Am. Chem. Soc. XXXX, XXX, XXX−XXX